scientific reports

Check for updates

OPEN

Magnetic and antibacterial properties of substituted cobalt spinel ferrite nanocomposites synthesized via henna green microwave hydrothermal method

Basmah Ghalib & Manal Hessien✉

A novel henna-green/microwave-assisted hydrothermal method was applied to synthesize cobalt-manganese spinel ferrite nanocomposites. This eco-friendly approach, utilizing henna extract as a capping agent, combined with a microwave-assisted hydrothermal technique, offers advantages such as environmental sustainability, time, and energy efficiency. Examined parameters included pH (10 ± 1), temperatures (175 ± 25 °C), durations (15, 30 ± 15 min), and forty milliliters of henna extract prepared with varying henna quantities (five, ten, or fifteen grams per hundred milliliters of water). Post-optimization, various substituents like nickel and chromium were explored. Samples were calcined at 500 °C, 700 °C, and 900 °C, and analyzed using Fourier Transform Infrared Spectroscopy (FTIR), X-ray Diffraction (XRD), Scanning Electron Microscopy (SEM), Transmission Electron Microscopy (TEM), X-ray photoelectron spectroscopy (XPS), and magnetic property assessments. XRD revealed a cubic face-centered spinel ferrite and hematite structure. SEM and TEM showed diverse morphologies (rod-like, flower-like, polygonal) influenced by synthesis conditions and substituents. XPS confirmed Co^{2+}, Mn^{2+}, Ni^{2+}, Fe^{3+}, and Cr^{3+} presence in the spinel lattice. The nanocomposites exhibited ferromagnetic behavior with saturation magnetization (M_s) values from 23.53 to 55.15 emu/g. Chromium substitution showed the best antimicrobial activity against *Escherichia coli*, *Staphylococcus aureus*, and *Candida albicans*. This study highlights the potential of the henna-green/microwave-assisted hydrothermal method for controlled synthesis of substituted cobalt spinel ferrite nanocomposites with tunable properties for various applications.

Keywords Henna aqueous extract, Green microwave-assisted hydrothermal, Cobalt-manganese spinel ferrite, Face-centered cubic phase, Magnetic properties

Spinel ferrites are a group of oxides that possess various properties including high saturation magnetization, electrical resistivity, low electrical loss, and chemical stability. For instance, the high saturation magnetization of spinel ferrites allows efficient magnetic field generation. In addition, their exceptional chemical stability ensures long-term device performance. They have extensive applications in millimeter-wave integrated circuitry, magnetic recording, magnetic sensors, hyperthermia, catalysis, and water pollutant photocatalysis[1–4]. Additionally, spinel ferrite has been used to adsorb dyes and as an antibacterial agent against various strains[5–8]. Furthermore, they have been employed as photocatalysts for dye degradation[5–9]. Magnetic materials are widely recognized for their valuable applications in hyperthermia and targeted drug delivery, as they can be easily manipulated using external magnetic fields. A crucial requirement for these materials is biocompatibility. Its magnetic properties and biocompatibility make it a promising candidate for magnetic resonance imaging applications[10]. Doped spinel ferrite nanoparticles have shown promising antimicrobial properties against various pathogens (Pseudomonas aeruginosa, Listeria monocytogenes, Candida albicans, Fusarium oxysporum, Escherichia coli and Staphylococcus aureus)[11,12].

In the field of ferrites with spinel structures, cobalt ferrite ($CoFe_2O_4$) is widely recognized as an inverse spinel structure that is typically characterized as a hard magnetic material owing to its notably high

Department of Chemistry, College of Science, King Faisal University, P.O. Box 400, 31982 Alahsa, Saudi Arabia. ✉email: mhessien@kfu.edu.sa

coercivity (H_c), considerable cubic magnetocrystalline anisotropy, and moderate saturation magnetization (M_s)[13,14]. The compound $MnFe_2O_4$, known as manganese ferrite, exhibits a partially inverse spinel structure and has attracted interest in the field of biomedicine due to its advantageous biocompatibility properties., superparamagnetic properties, and capacity for monitoring using an external magnetic field. Additionally, $MnFe_2O_4$ exhibits attractive properties, such as heat resistance, non-corrosiveness, environmental friendliness, non-toxicity, and high shock resistance[14,15]. Furthermore, Mn substitution in cobalt ferrite is believed to result in a magnetomechanical effect and heightened sensitivity to stress, making it a promising candidate for use in stress-sensor applications. Manganese offers several advantages, including the capacity to exist in various oxidation states, good luminescence properties, and a significant magnetic moment for Mn^{2+}. Consequently, manganese-cobalt ferrite has garnered considerable interest from researchers who have extensively examined its properties[16–18].

Nickel-doped cobalt ferrites ($NiCoFe_2O_4$) exhibit several advantageous properties that render them suitable magnetic fillers for electromagnetic interference (EMI) shielding nanocomposites. These characteristics encompass substantial permittivity and permeability, reduced magnetocrystalline anisotropy, appropriate resistivity (ranging from ~ 10^5 to 10^4 Ω cm^{-1}), elevated Curie temperature (approximately 800 K), and high chemical stability. These intrinsic qualities contribute to their efficacy in such applications[19]. The incorporation of Cr^{3+} ions, a transition metal ion species, into $CoFe_2O_4$ significantly alters its magnetic characteristics. This alteration occurs because Cr^{3+} ions consistently occupy the Fe^{3+} (B) site and influences magnetic parameters such as remanence and coercivity in chromium-substituted $CoFe_2O_4$ nanoparticles[20]. Singh et al. observed that the replacement of Fe^{3+} by Cr^{3+} in the $CoFe_2O_4$ matrix reduced the O_2 overpotential significantly[21]. The decrease in r_A and r_B is due to the replacement of Fe^{3+} ions (0.67 Å) by smaller Cr^{3+}ions (0.63 Å) at both sites. Cation distribution studies revealed that Co^{2+} and Fe^{3+} occupy both A and B sites, whereas Cr^{3+} ions occupy only B site. Saturation magnetization, remanence magnetization and coercivity decreases with increase in chromium substitution[22].

The hematite α-Fe_2O_3 is the most stable iron oxide having rhombohedral structure with 2.2 eV as an indirect band gap[17,18]. The magnetic ordering of α-Fe_2O_3 is antiferromagnetic. The spins lie along [111] axis to exhibit α-Fe_2O_3 as a pure uniaxial antiferromagnet[23]. A significant advantage of $NiFe_2O_4$/α-Fe_2O_3 and $CoFe_2O_4$/α-Fe_2O_3 nanocomposites is their capacity to maintain stable magnetization at elevated temperatures. This phenomenon can be attributed to the antiferromagnetic nature of α-Fe_2O_3 in conjunction with the ferrimagnetic properties of $NiFe_2O_4$ and $CoFe_2O_4$[23]. According to Naoe et al.[24], the antiferromagnetic properties of α-Fe_2O_3 in the plane contribute to the alignment of the quasi in-plane magnetization of $CoFe_2O_4$ through magnetic interactions. This characteristic is advantageous for longitudinal recovery recording media. The enhanced microwave absorption properties of the α-Fe_2O_3/$CoFe_2O_4$ composite have been documented in the literature[25]. Research conducted by Huang et al.[26] examined $NiFe_2O_4$/α- Fe_2O_3 as an anode material for electrochemical applications. Their findings revealed that this material exhibited significant reversible charge–discharge capacity, outstanding cycling durability, and exceptional rate performance.

Nanospinel oxides can be prepared using different approaches, such as the hydrothermal method, microwave combustion, citrate sol–gel, co-precipitation, and micelle methods[5,27–30]. The microwave-hydrothermal method integrates the advantages of both hydrothermal and microwave techniques. It incorporates the hydrothermal approach's simplicity, processability, cost-effectiveness, shortened reaction duration, and reduced synthesis temperature. Additionally, it leverages the microwave technique's energy efficiency, non-contact operation, and potential for scaling up[31–34]. Manohar et al. prepared Zn–Ni spinel ferrite using a solvothermal method. Magnetism increased with increasing Ni^{2+} concentration. The monodisperse spinel ferrite nanoparticles exhibited good heat efficiency and generated hyperthermia temperatures exceeding 43 °C. Moreover, the prepared spinel ferrites have been used to remove methylene blue as a model organic pollutant under visible light[4]. A. Dhiwahar et al. prepared Cu-Ni ferrite via microwave combustion. The synthesis methods in the solution phase are highly sensitive to the pH, which directly affects the formation of ferrite particles, their particle size, and the degree of crystallinity. As a result, the pH plays a critical role in determining the physical and chemical properties of ferrite nanoparticles[35].

The properties of nanospinel oxides strongly depend on their size distributions and morphologies. The size distribution and morphology can be tuned through many factors, such as pH during the precipitation step and temperature, and time during the microwave-assisted hydrothermal step[27,36]. Aggregation, a common phenomenon observed in nanomaterials, diminishes their effective surface area. Capping agents offer a solution by hindering aggregation and directing the growth of nanomaterials, thereby enabling precise control of their size and morphology[37]. Capping agents include surfactants, polymers, and natural compounds. Natural compounds can be sourced from a variety of biological materials, including leaves, fruits, fruits, roots, and seeds, as well as eco-friendly components such as carbohydrates, vital nutrients, microbes, and biopolymers[37].

Various reviews have discussed the plant-mediated green synthesis of spinels[6,38,39]. A. Chaudhari et al. prepared manganese ferrite by combustion method using plant extract as a fuel[7]. Eco-friendly copper ferrite nanoparticles were prepared via green synthesis using *Nasturtium officinale* extract[40]. In this study, *Nepeta bornmuelleri* was used for the synthesis of ferrite spinel nanosheets, which is a cost-effective and eco-friendly solution. The results indicate that the nanosheets had a size range of less than 100 nm[41].

Henna, also referred to as Lawsonia inermis, is a small tree or shrub that is native to North Africa, Southwest Asia, and Northern Asia. It has been utilized as a natural dye and cosmetic since the Bronze Age[42]. Henna is a natural substance rich in antioxidants, particularly polyphenols. The primary active ingredient in Henna leaves is lawsone (2-hydroxy-1,4-naphthoquinone), also known as hennotannic acid, which is a reddish-orange dye that gives the plant color[43]. Research on phytochemicals has revealed that it contains a variety of compounds, including aromatic compounds, saponins, alkaloids, flavonoids, phenols, tannins, coumarins, lignans, and gallic acid, among others[44].

Despite the potential of substituted cobalt ferrite in various fields, limited research has been conducted in studying synthesis conditions for preparing $Co_{0.5}Mn_{0.5}Fe_2O_4$ using henna extract as a capping agent. Additionally, there is no existing data on combining henna extract with the microwave-assisted hydrothermal method in the synthesis of spinel ferrite. In this study, we present a novel method for synthesizing $Co_{0.5}Mn_{0.5}Fe_2O_4$ under various conditions, including henna extract concentration, pH, time, and temperature. The eco-friendly synthesis approach utilizing henna extract was combined with a microwave-assisted hydrothermal technique. Following optimization of synthesis conditions, various substituents such as nickel and chromium were investigated. The synthesized samples were characterized using X-ray diffraction (XRD), infrared spectroscopy (FTIR), UV–Vis spectroscopy, scanning electron microscopy (SEM), transmission electron microscopy (TEM), and X-ray photoelectron spectroscopy (XPS) analysis. Antibacterial activity and magnetic property measurements were performed to examine the samples prepared under optimum conditions.

Materials and methods

Materials

Ferric chloride ($FeCl_3{\cdot}6H_2O$, 98%), manganese chloride hexahydrate ($MnCl_2{\cdot}6H_2O$, 97%), cobalt chloride hexahydrate ($CoCl_2{\cdot}6H_2O$, 98%), $CrCl_3{\cdot}6H_2O$, $NiCl_2{\cdot}6H_2O$, and KOH were purchased from Sigma-Aldrich. Henna leaves were collected from a local farm in Alhasa at coordinates (25.9326° N, 49.6640° E).

Henna extraction

The henna leaves were first cleaned and dried in the shade (at room temperature for 7 days) and then ground using a grinder. A solution was prepared by combining henna powder with deionized water in a 1:10 ratio (1 g of powder per 10 ml of water). The resulting mixture underwent sonication for 3 h at a temperature of 70 °C. Subsequently, the solution was filtered using Whatman filter paper to obtain the final extract. The extract was then stored in a refrigerator at 4 °C and labeled as "henna extract."

Microwave-assisted hydrothermal synthesis

Metal precursors with a molar ratio of 1:1:4 for Mn:Co:Fe salts, with a total concentration of 0.02 M solution, were prepared. Volume ratio of henna extract solution to metal precursors solution was 1:4. The sample codes and corresponding synthesis conditions are listed in Table 1. The CCF, MCF, and NCF codes were used for samples prepared with a molar ratio of 1:1:4 for Cr:Co:Fe, Mn:Co:Fe, and Ni:Co:Fe salts; respectively. The synthesis process involved combining a precise quantity of the metal precursor with purified water. Following this, 40 mL of henna extract was introduced to 160 mL of the salt solution. The mixture's pH was then adjusted using KOH solution. The resulting hydroxide precipitate was relocated to a Teflon container and exposed to microwave radiation at a specified temperature for a designated time period. To carry out this procedure, a Titan MPS microwave system (Perkin Elmer) capable of delivering up to 2700 W of power, along with ten Teflon vessels (each containing 50 mL), was utilized. The received powder was dried then calcined at 500 °C, 700 °C, and 900 °C. A schematic representation of the synthetic method is presented in Scheme 1.

After removing the Teflon container from the microwave, the specimen was moved to a beaker and surplus water was eliminated. The sample underwent further processing employing a PowerSonic 405 instrument (operating at 40 kHz frequency and 350 Watt power), which performed sonication for 90 min in 50 mL of distilled water. Subsequently, the solid component was left to naturally descend due to gravitational forces for 24 h. The liquid was then poured off, and 20 mL of ethanol was introduced. This process was repeated, and the resulting sample was dehydrated in an oven at 100 °C for 24 h. Lastly, the specimens were subjected to heating

Sample Code	B: pH	C: Temp (°C)	D: Time (min.)	E: Extract vol (g of henna/Vol. Water)
Effect of pH				
9B	***9***	200	30	40 mL (1 g/10 mL)
10B	***10***	200	30	40 mL (1 g/10 mL)
11B	***11***	200	30	40 mL (1 g/10 mL)
Effect of temperature				
150C	10	***150***	30	40 mL (1 g/10 mL)
175C	10	***175***	30	40 mL (1 g/10 mL)
200C	10	***200***	30	40 mL (1 g/10 mL)
Effect of time				
15T	10	200	***15***	40 mL (1 g/10 mL)
30T	10	200	***30***	40 mL (1 g/10 mL)
45T	10	200	***45***	40 mL (1 g/10 mL)
Effect of extract concentration				
WE	10	200	30	–
1E	10	200	30	40 mL (**0.5 g**/10 mL)
2E	10	200	30	40 mL (**1 g**/10 mL)
3E	10	200	30	40 mL (**1.5 g**/10 mL)

Table 1. Codes of samples prepared under various synthesis conditions.

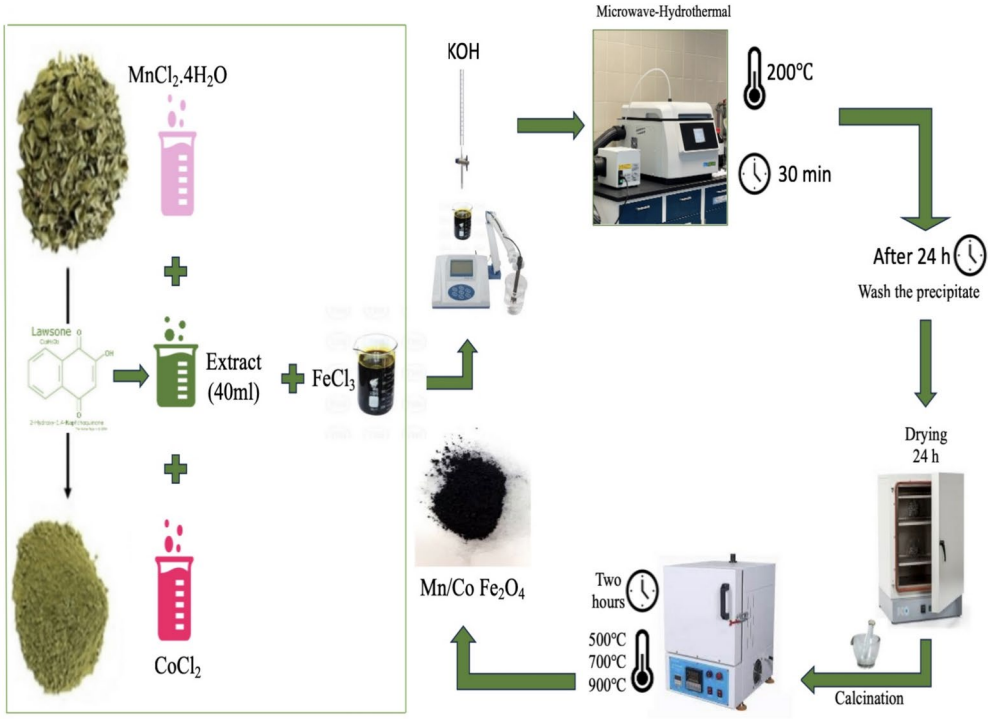

Scheme 1. Synthesis of cobalt-manganese spinel ferrite nanocomposites.

at 500 °C for 2 h in a Sanwood Box-type Resistance Furnace, operating at 2.5 kW, to eliminate any remaining organic matter.

Materials characterization

A Cary 630 FT-IR spectrophotometer was employed to acquire the FTIR spectra of the spinel ferrite. X-ray diffraction (XRD) analysis was performed using a Bruker D8 X-ray diffractometer to identify the crystalline phases present in the sample. The apparatus utilized copper K-alpha radiation filtered through nickel and a graphite monochromator to generate X-rays. These X-rays had a wavelength of 1.54060 Å and were produced at settings of 35 kV and 25 mA. The analysis encompassed a sweep across glancing angles ranging from 10° to 60°, utilizing increments of 0.02° and maintaining a precision of ≤ 0.001°.

The surface morphology was thoroughly analyzed using a Scanning Electron Microscope (SEM). The specific instrument employed for this investigation was the Quanta FEG250, a device produced in Holland. The apparatus operates with an accelerating voltage of 30 kV and is capable of magnifying images up to 400,000 times their original size. To conduct an in-depth transmission electron microscopy (TEM) examination, scientists utilized a JEOL JEM-2100 transmission electron microscope (JEOL, Japan) with an accelerating voltage of 200 kV. To prepare the TEM sample, a minute amount of the colloidal suspension was deposited onto a TEM grid and allowed to dry naturally at room temperature. Following the complete evaporation of the solvent, the grid was immediately subjected to TEM analysis.

A K-Alpha device manufactured by Thermo-Fisher Scientific, a corporation based in Waltham, Massachusetts, USA, was utilized to conduct X-ray photoelectron spectroscopy (XPS) analysis. The study employed Al Kα X-ray radiation with a single wavelength, spanning from − 10 to 1350 eV. The radiation was focused to a 400 spot size and conducted under a pressure of 10–9 mbar. For the complete spectrum analysis, the pass energy was configured at 200 eV, while the narrow spectrum examination used a pass energy of 50 eV. The binding energy of the C1s peak at 284.4 eV was used to establish the charge correction. A Lake Shore VSM 7410 model equipped with a 3 Tesla magnet was employed to perform magnetic property measurements at ambient temperature.

To assess antimicrobial activity, researchers measured the optical density (OD) using a wavelength of 600 nm. The experimental approach utilized cultures of bacteria and fungi, specifically the Gram-negative bacterium Escherichia coli (ATCC25922), the Gram-positive bacterium Staphylococcus aureus (ATCC 6538), and the disease-causing yeast Candida albicans (ATCC 10231). These microorganisms were cultivated and preserved on slanted nutrient agar media. Fresh working stock cultures were prepared by aseptically transferring each culture into 5.0 mL of sterile nutrient broth and incubating overnight at 37 °C. The bacterial suspension was calibrated to match approximately 0.5 McFarland standard, which corresponds to a concentration of 1.5×108 colony-forming units per milliliter. Nutrient broth medium (20.0 mL) was placed in 100.0 mL conical flasks, along with 25.0 µL of the prepared inoculum suspensions. These flasks were then inoculated with 25 µL of bacterial and fungal suspensions. The sample was then introduced to the microorganisms, which were incubated at 37 °C for 24 h. The proliferation of disease-causing bacterial strains was assessed by observing the absorbance at a

wavelength of 600 nm. The evaluation of antimicrobial efficacy involved comparing the percentage reduction in relative optical density (OD) of treated pathogenic strains against the control. The results were quantified using the provided mathematical formula[14,15].

$$\text{Relative reduction optical density } [\text{OD Reduction } (\%)] = (\text{A} - \text{ B } /\text{A}) \times 100,$$

where A is the number of microorganisms present on control flask contains bacterial strain only without any thing. B is the number of microorganisms present on shake flask for tested samples.

Results and discussion

FTIR characterization of samples prepared under various conditions

Figure 1a displays the infrared spectroscopic analysis of henna extract and sample 10 B after calcination at 500 °C, 700 °C, and 900 °C and Fig. 1b is the magnification of FTIR. The FTIR analysis of aqueous henna extract displayed a broad band ranging from 2800 to 3600 cm^{-1}, which could be attributed to the stretching vibration of the aromatic and aliphatic OH groups present in henna. It is important to note that the FTIR spectrum of the henna extract displays a very broad band between 2800 and 3600 cm^{-1}, which may overlap with the band (3000–3100 cm^{-1}) for the stretching of aromatic and aliphatic compounds. In addition, an acute, needle-like peak was detected in the range of 1500–1700 cm^{-1}, which suggests the presence of carbonyl groups or bending of aromatic structures. Additionally, a significantly wide band was detected in the region below 1000 cm^{-1}, which could be associated with the bending of aromatic C–H, C=C, or C–O–C bonds. The findings of the FTIR analysis of henna extract, as reported in the literature, indicate the presence of flavonoids, tannins, and terpenoids in the extract[45].

The FTIR spectra of $Co_{0.5}Mn_{0.5}Fe_2O_4$ after calcination at different temperatures are displayed in Fig. 1a,b.It is evident from the figure that the disappearance of the extract bands due to calcination and the emergence of well-defined peaks between 400 and 600 cm^{-1} suggest the formation of M–O bonds. There are two characteristic bands at 445 cm^{-1} and 535 cm^{-1} for the octahedral and tetrahedral sites, respectively. The variation in the vibrational frequencies can be explained by the longer bond length between the oxygen and metal ions in the tetrahedral positions. This elongation is affected by several factors, including the strength of the bonding force, mass of the cation, and distance between the oxygen and metal ions. The interaction between the metal and oxygen ions is responsible for this phenomenon, with the intensity of the bonding force and spatial separation between the ions playing crucial roles. In addition, the mass of the cation determines the length of the bond, which in turn influences the vibrational frequency of the system[5,7,8,46,47]. The synthesis of $Co_{0.5}Mn_{0.5}Fe_2O_4$ nanoparticles has been successfully verified by these findings, which also offer important information about their structural properties, particularly the establishment of metal–oxygen bonds in both octahedral and tetrahedral positions.

XRD characterization of samples prepared under various conditions

The XRD patterns of $Co_{0.5}Mn_{0.5}Fe_2O_4$ spinel ferrite samples, calcined at 900 °C, under various synthesis conditions, are depicted in Fig. 2. All the samples exhibited peaks at 2θ ~ 30.09°, 35.37°, 37.11°, 43.29°, 53.36°, and 57.02° for the (220), (311), (222), (400), (422), and (511) planes of spinel ferrite with a cubic face-centered structure according to JCPDS card No. 22-1086[48–50]. The (311) plane exhibited the highest peak intensity,

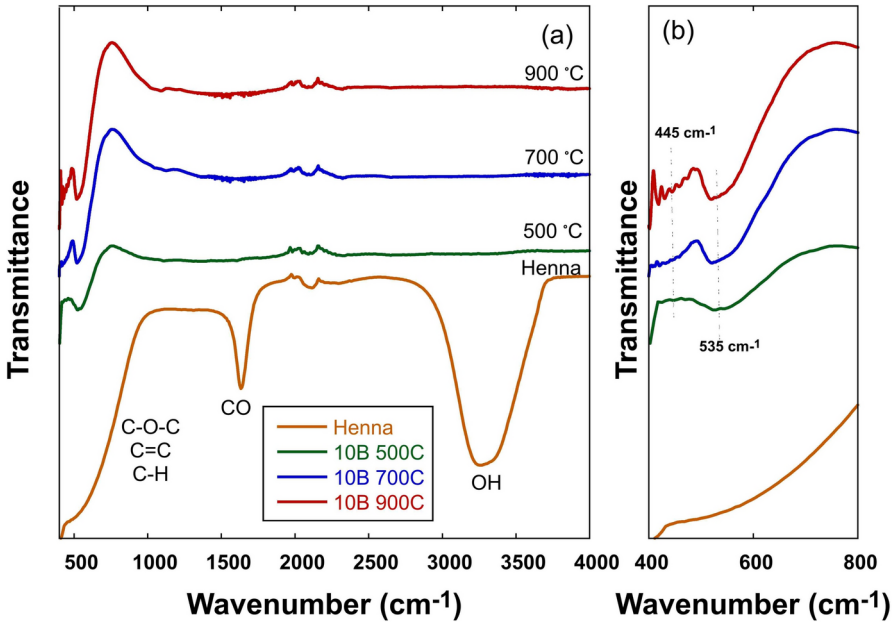

Fig. 1. FTIR spectra of (**a**) henna extract, and sample 10 B after calcination at 500 °C, 700 °C, and 900 °C and (**b**) the magnification of FTIR.

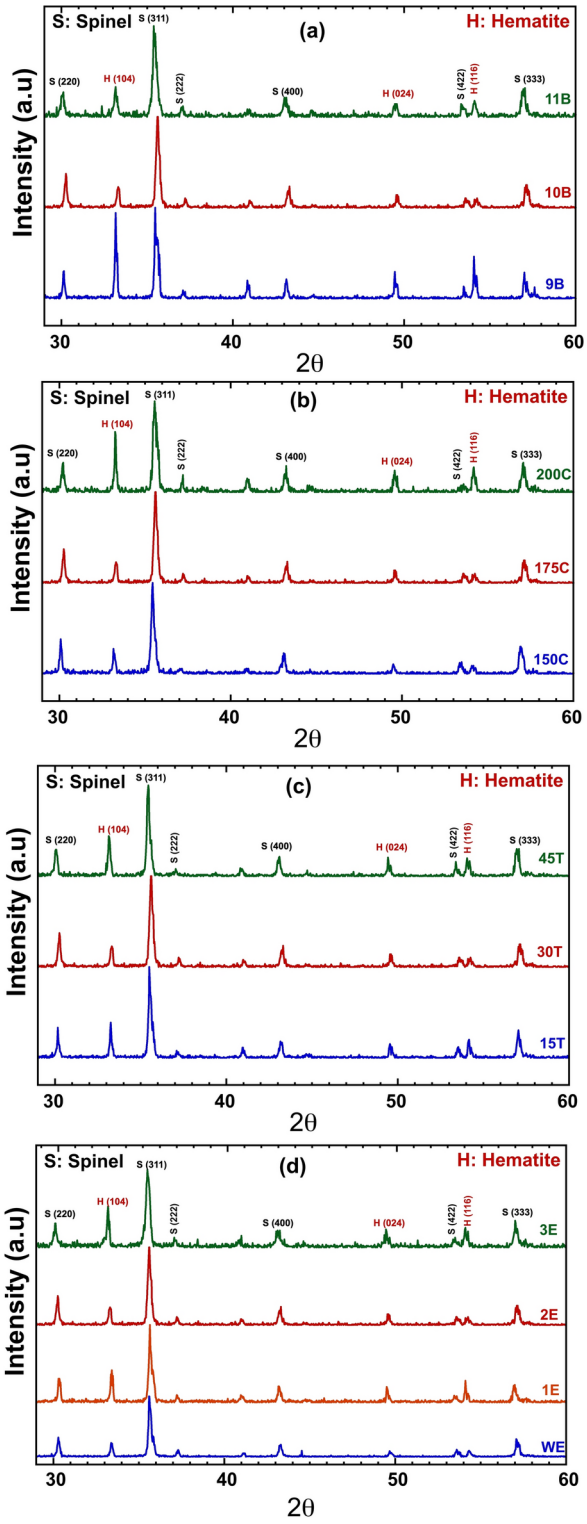

Fig. 2. XRD diffractograms of cobalt-manganese spinel ferrite samples prepared under different (**a**) pH, (**b**) temperature, (**c**) time, and (**d**) extract concentrations.

suggesting that nanoparticles were prevalent in the (311) orientation of the diffraction plane. Moreover, the samples exhibited peaks at 2θ ~ 33.07°, 49.55°, and 54.07° for the (104), (024), and (116) orientations of hematite according to JCPDS card No. 89-0598[51,52]. The appearance of α-Fe_2O_3 is believed to result from the thermal decomposition and oxidation processes that occurred during the annealing stage (i.e., calcination at 900 °C). According to certain studies, this phase vanishes after heat treatment at elevated temperatures[53]. These findings

emphasize the importance of carefully controlled processing conditions for tailoring the crystalline properties for specific applications.

The synthesis conditions of the samples affected the compositions of the $Co_{0.5}Mn_{0.5}Fe_2O_4$ spinel ferrite/hematite composites. The presence of hematite was observed by examining the primary peak of the hematite phase at approximately $2\theta = 33.07°$ for the (104) orientation. The intensity of the (104) peak reached its maximum under conditions across different samples. This occurred when the pH was adjusted to 9 in sample 9B. Among samples prepared at various temperatures, the peak intensity was greatest when synthesis took place at 200 °C in sample 200C. The (104) peak was most pronounced in sample 45 T, which underwent a 45-min synthesis process. Finally, the peak attained its highest intensity in sample 3E, which utilized 40 mL of a stock solution prepared by mixing 1.5 g of henna with 10 mL of water. Samples 10B, 175C, 30 T, and 2E exhibited the lowest intensity of the (104) peak. These specimens were produced under specific conditions: a pH level of 10, a temperature of 175 °C, a reaction duration of 30 min, and using 40 mL of a solution made by combining 1 g of henna with 10 mL of water. Because cobalt is more soluble than iron, it requires a higher pH to precipitate. The presence of cobalt as a non-precipitated species results in the precipitation of iron as hematite[54,55]. These findings demonstrate the critical role of synthesis parameters, particularly pH, temperature, time, and extract concentration, in optimizing the formation and intensity of the hematite (104) peak relative to spinel ferrite, which has important implications for the controlled synthesis of spinel ferrite composites using henna extract.

Microstructure characterization of samples prepared under various conditions

The morphological analysis of the cobalt-manganese spinel ferrite was significantly examined through SEM examination. Figure 3a shows the SEM image of the WE sample, which was prepared at a pH 10, 30 min, synthesis temperature of 200 °C, and without the henna extract. The sample is inhomogeneous and highly agglomerated. Figure 3b–d shows the SEM image of sample 1E, 2E, and 3E which were prepared at pH 10, 30 min synthesis time, 200 °C synthesis temperature, and with different concentration of henna extract. Sample 1E (0.5 g/10 mL of henna extract) exhibited a homogenous and well-dispersed short rod-like structure compared with the sample WE. Increasing the concentration of henna extract to (1 g/10 mL) in sample 2E results in a flower-shape homogenous structure. A further increase in henna extract (1.5 g/10 mL) in sample 3E results in a well-dispersed homogenous polygonal structure indicating the role of henna extract. These results suggest that henna

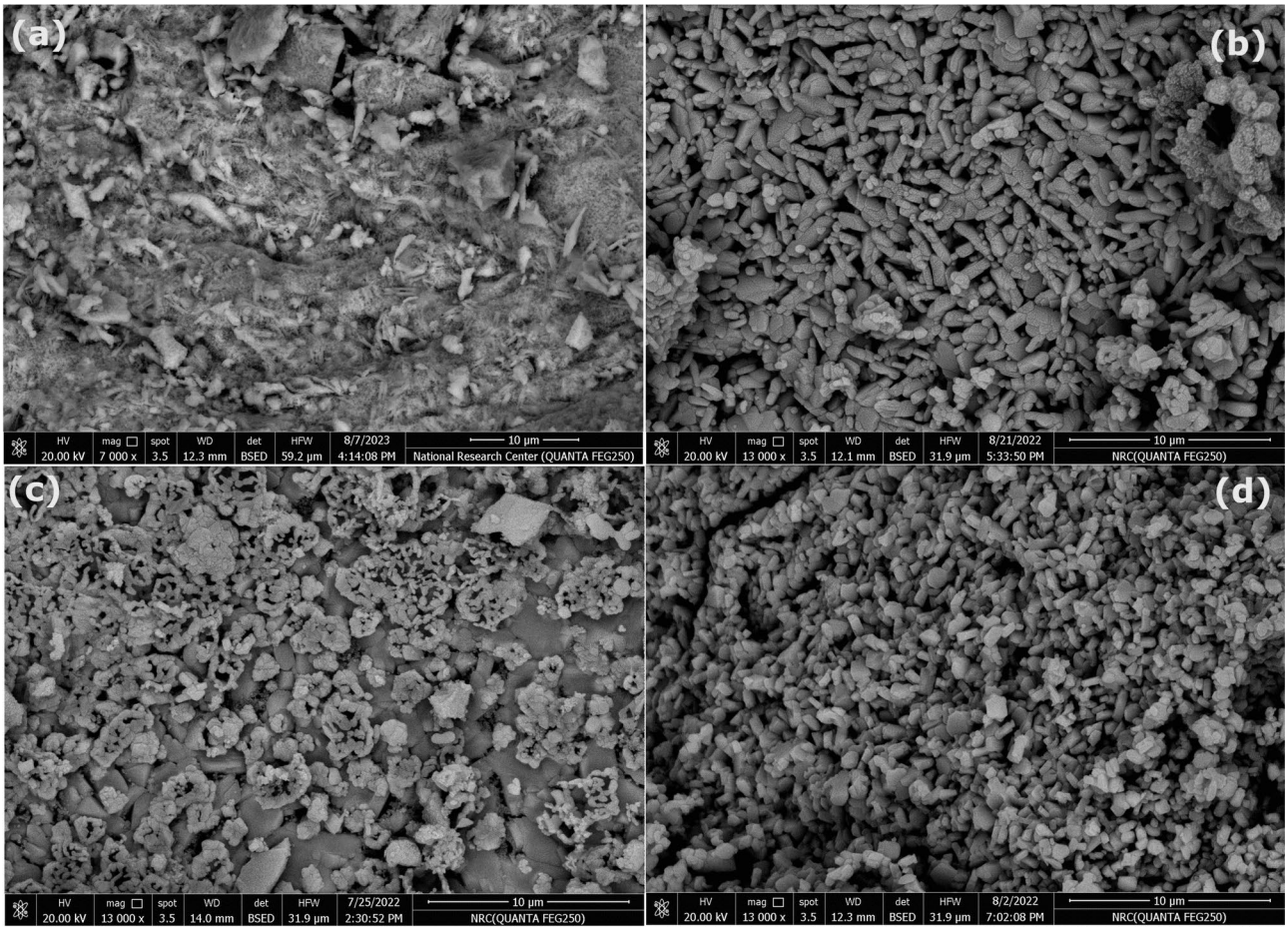

Fig. 3. SEM images of samples prepared under different extract concentration (**a**) WE, (**b**) 1E, (**c**) 2E, and (**d**) 3E.

content plays a crucial role in the nucleation and growth of ferrite nanocomposites, ultimately affecting the morphology of the spinel ferrite. Terpenoids and flavanones in henna extract act as capping agents, preventing agglomeration. Phytoconstituents regulate the growth of metal oxides and affect their morphologies[42,44,45,56]. The extract concentration is crucial in determining phytoconstituent levels, influencing spinel growth, and reducing particle size[43,57]. This study highlights the role of the extract in minimizing the particle size.

The effect of pH on the morphological features of cobalt-manganese spinel ferrite during the synthesis process was investigated using scanning electron microscopy (SEM). Figure 4a,b show SEM images of samples 9 B and 11 B prepared at pH 9 and 11, respectively. The morphology of sample 9 B was homogenous and well-dispersed in a polygonal shape. Increasing the pH to 11 in sample 11 B resulted in an elongated worm-gear shape. Kershi et al. prepared cobalt ferrite with co-precipitation method at pH ranging between 9 and 13. They reported that higher pH values resulted in increased particle size[58].

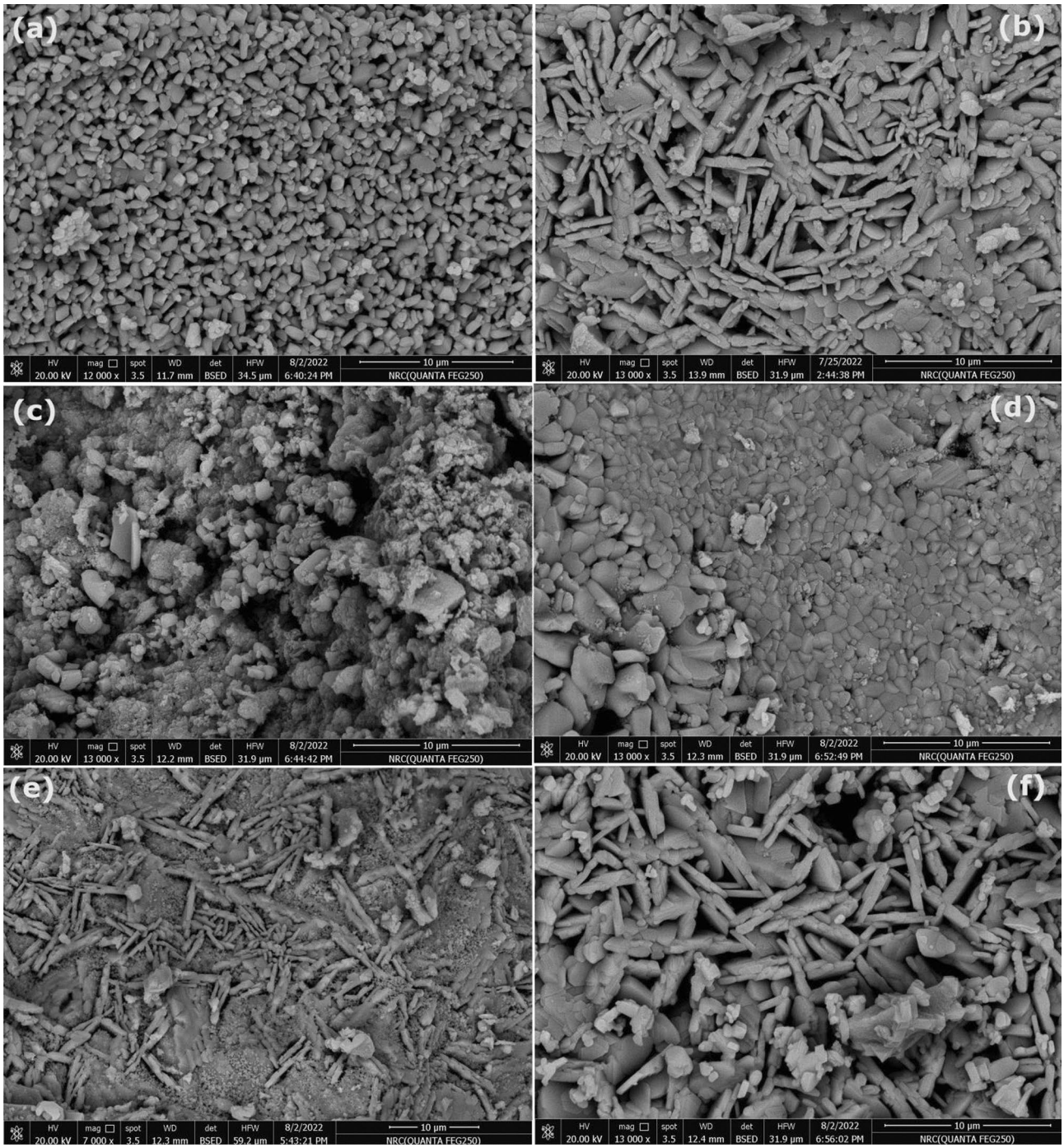

Fig. 4. SEM images of samples prepared under (**a**) pH 9, (**b**) pH 11, (**c**) 150 °C, (**d**) 175 °C, (**e**) 15 min and (**d**) 45 min.

Figure 4c,d illustrate how temperature variations during microwave-hydrothermal synthesis influence the morphological characteristics of spinel ferrite. Sample 150C shows a morphology of polydisperse agglomerated particles compared to the well-dispersed polygonal shape in sample 175C. Figure 4e,f illustrate how the length of the synthesis process affects the morphological characteristics of the cobalt-manganese spinel ferrite. Sample 15 T shows the morphology of some elongated structures immersed in polydisperse agglomerated particles compared to elongated worm gears when the synthesis time was increased to 45 min in sample 45 T. The change in grain shape and size with increasing time and temperature of the microwave-hydrothermal method may be attributed to the dissolution and redeposition steps in the Ostwald ripping process[54].

Figure 5a shows the TEM images of Sample WE, showing a bimodal size structure with large quasi-spherical particles in the size range of 50–215 nm and smaller spherical particles in the size range of 15–20 nm. Sample 1E, which is prepared under the same conditions as sample WE but with 40 mL henna extract of concentration (0.5 g/10 mL), showed rod-like structure with ~ 40 nm width and 200 nm length, as depicted in Fig. 5b. Increasing the concentration of henna extract to 1 g/10 mL in sample 2E resulted in a decrease in the size of particles observed in sample 1E and the formation of a polygonal shape of ~ 35 nm, as depicted in Fig. 5c. Further increase in the concentration of henna extract to 1.5 g/10 mL resulted in smaller particle size ~ 9 nm with spherical shape, as depicted in Fig. 5d of sample 3E. The concentration of henna extract plays a crucial role

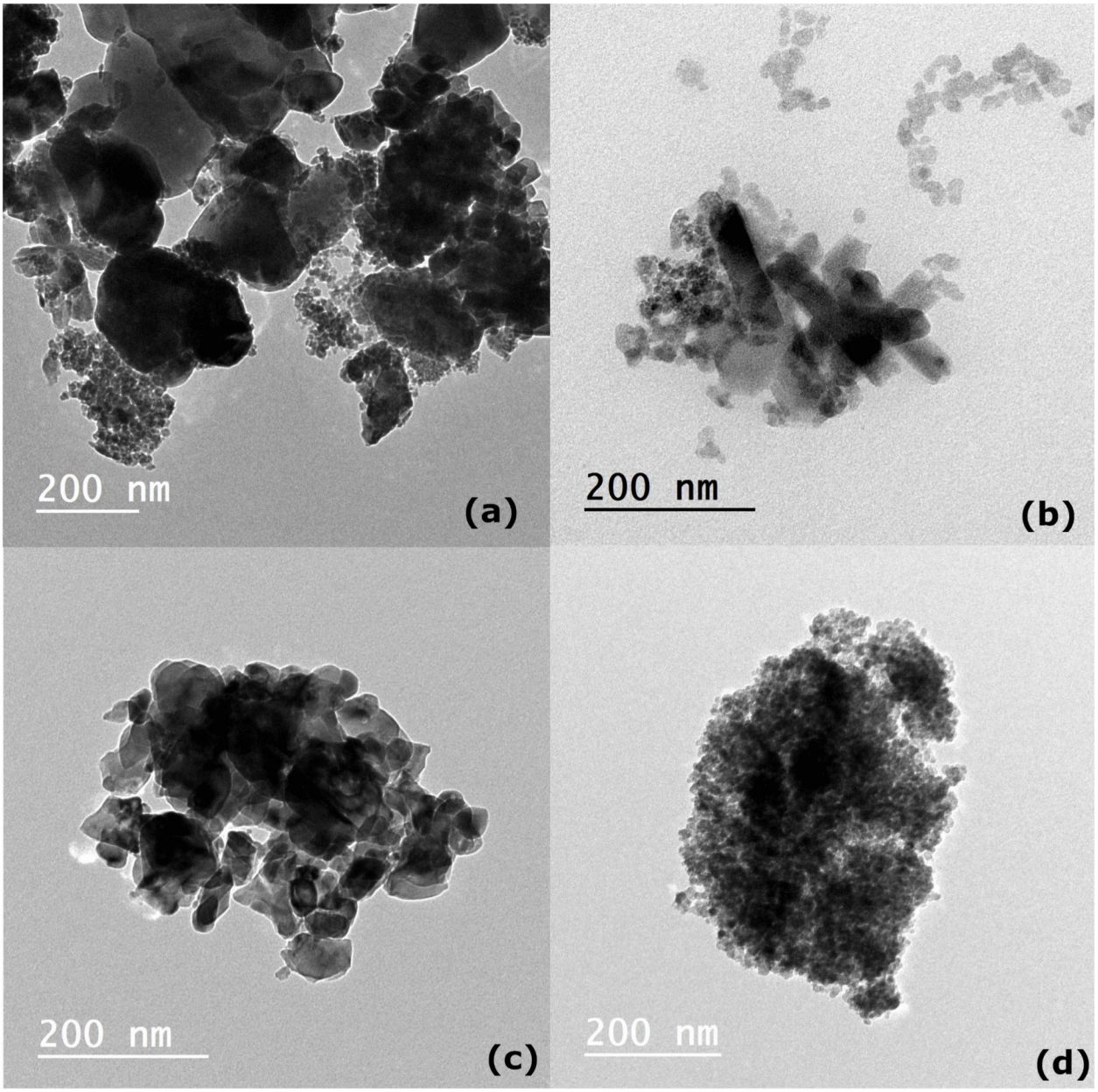

Fig. 5. TEM images of samples prepared under different extract concentration (**a**) WE, (**b**) 1E, (**c**) 2E, and (**d**) 3E.

in the formation and development of nanocomposites, influencing the dimensions and form of spinel ferrite. Compounds such as terpenoids and flavanones found in henna extract function as capping agents, inhibiting particles clumping. The phytochemicals present in the extract controlled the growth of metal oxides, thereby affecting their morphology. Alkaloids and flavonoids in henna leaf extract serve as capping agents[42,44,45,56], facilitating uniform particle growth and controlling particle dimensions. The amount of extract used determines the level of phytoconstituents, which affects spinel growth and leads to reduced particle dimensions[43,57]. This study emphasizes the effect of the extract on decreasing particle size.

At pH 9 (Fig. 6a), the image displays homogenous and well-dispersed polygonal particles with sizes in the range 11–17 nm. Increasing the pH to 11 in sample 11 B resulted in an elongated worm gear shape with a larger size in the range of 300–400 nm, as depicted in Fig. 6b. Increasing the microwave treatment temperature from 150 to 175 °C resulted in a higher growth rate and larger particle size, as shown in Fig. 6c,d. Sample 150C showed a morphology of agglomerated particles with sizes in the ranges of 25–35 nm and 60–120 nm. Sample 175C showed a well-dispersed polygonal shape in the range of 50–170 nm. The impact of the duration of the synthesis process on the morphological features of the cobalt-manganese spinel ferrite is depicted in Fig. 6e,f. Sample 15 T shows the morphology of elongated structures immersed in polydisperse agglomerated particles with sizes in the range of 50–100 nm. Sample 45 T elongated worm gears when the synthesis time was increased to 45 min with size 50–90 nm.

Given the associated outcomes, it is possible to propose a mechanism for the formation of cobalt-manganese spinel ferrite. The first step is the dissolution of metal salt precursors to form a multiaqua cation complex (Eq. 1). Then, the multiaqua cation complexes undergo hydration and hydroxide formation, which are affected by the pH (Eq. 2). Subsequently, the dehydration and formation of oxides undergo nucleation and growth, respectively (Eq. 3). Growth can occur via diffusion, Ostwald ripening, or aggregation. In this step, time, temperature, and extract influence the growth pathways. The occurrence of one type of growth depends on the synthesis conditions[13,54,59]. The impact of synthesis temperature on the reaction kinetics and nucleation rate of this approach should not be overlooked. In general, it is well-known that the properties of reagents, such as their solubility and reactivity, can change at high temperatures[13]. The presence of terpenoids and flavanones in henna extract can serve as a capping agent surrounding the growing particles, inhibiting subsequent growth. Phytoconstituents act as capping agents and regulate the growth of spinels, which may influence their morphology. Experimental variables such as pH, growth duration, and growth temperature are the primary factors that determine the size and quality of spinel ferrite[60]. The use of a henna-green/microwave-assisted hydrothermal technique in the synthesis process was characterized by environmentally friendly reaction conditions. This technique utilizes water as the primary solvent, operates at reduced temperatures, and avoids the use of harmful chemicals or dangerous solvents.The process benefits from microwave radiation, which generates localized hotspots and facilitates the nucleation and growth of spinel ferrite nanoparticles[54,59].

$$MCl_x.6H_2O \rightarrow^{H2O} \left[M\left(H_2O\right)_6\right]^{x+}_{aq} + xCl^- \quad (1)$$

$$\left[M\left(H_2O\right)_6\right]^{x+}_{aq} \rightarrow^{NaOH} \left[Mn\left(OH\right)_y\right]^{x-y} \rightarrow^{NaOH} M\left(OH\right)_{xs} \rightarrow^{NaOH} \left[M\left(OH\right)_{x+1}\right]^-_{aq} \quad (2)$$

$$\left[Mn\left(OH\right)_3\right]^-_{aq} + \left[Co\left(OH\right)_3\right]^-_{aq} + \left[Fe\left(OH\right)_4\right]^-_{aq} \rightarrow Mn/CoFe_2O_{4(s)} + H_2O_{(l)} + OH^- \quad (3)$$

where M = Mn^{2+}, Co^{2+}, Fe^{3+}.

XRD of samples prepared with different dopants

Figure 7 illustrates the XRD patterns of CCF, MCF, and NCF samples where cobalt spinel ferrite were substituted with chromium, manganese, and nickel; respectively, after calcination at 900 °C. The diffractograms revealed characteristic peaks at 2θ ~ 30.09°, 35.37°, 37.11°, 43.29°, 53.36°, and 57.02°, corresponding to the (220), (311), (400), (422), and (511) planes, respectively. These peaks are indicative of a spinel ferrite structure with a cubic face-centered lattice, as confirmed by JCPDS card No. 82-1042[48–50]. Additionally, the samples CCF and MCF exhibited diffraction peaks at 2θ angles of approximately 33.07°, 49.55°, and 54.07°, corresponding to the (104), (024), and (116) crystallographic orientations of hematite; respectively according to JCPDS card No. 89-0598[51,52]. These diffraction patterns provide evidence for the absence of hematite in the NCF sample, indicating successful stability of nickel cobalt spinel ferrite nanoparticles.

Cobalt ferrite with nickel substitution generates a pure cubic spinel structure due to several factors: nickel's consistent + 2 oxidation state in spinels, its preference for octahedral sites, and its ionic radius (0.69 Å) being comparable to that of Co^{2+} (0.74 Å). These characteristics facilitate substitution and enhance the structure's resistance to high-temperature decomposition. In contrast, substituting manganese or chromium results in a combination of cubic spinel and hematite phases. This occurs because manganese can exhibit multiple oxidation states (+2, +3, +4), while chromium's oxidation state can vary (+2, +3, +6), rendering them susceptible to forming secondary phases such as hematite. Their ionic radii (Mn^{2+}: 0.83 Å; Cr^{3+}: 0.62 Å) induce lattice distortion and instability. Hematite formation occurs during thermal decomposition and oxidation at elevated temperatures, such as during 900 °C calcination. In essence, the stability, ionic radius, and cation distribution of Ni^{2+} promote a pure cubic spinel phase. Conversely, the oxidation states and ionic radii of Mn and Cr disrupt the spinel structure, facilitating hematite formation under specific synthesis conditions.

Microstructural characterization of samples prepared with different dopants

SEM analysis was conducted on calcined samples to examine the surface morphology of spinel ferrite. The SEM images and EDAX analyses of cobalt-ferrite spinel doped with various elements such as chromium, manganese,

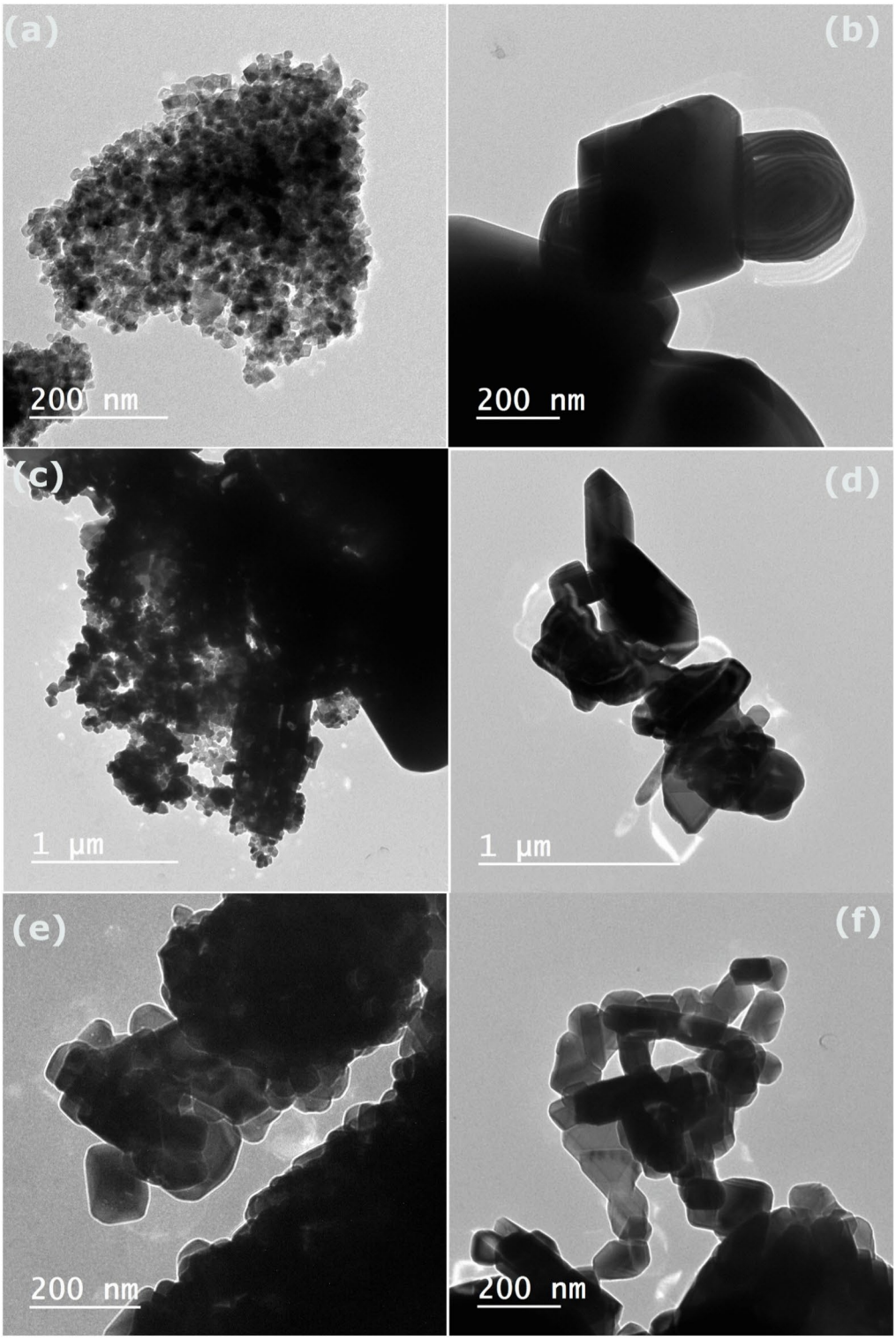

Fig. 6. TEM images of samples prepared under (**a**) pH 9, (**b**) pH 11, (**c**) 150 °C, (**d**) 175 °C, (**e**) 15 min and (b) 45 min.

and nickel are displayed in Fig. 8. Sample CCF in Fig. 8a shows smooth polygonal structure, chromium doping often results in more angular or faceted particles and show reduced agglomeration due to surface charge effects. Figure 8b shows sample MCF exhibiting a highly agglomerated structure of stacked sheets with interspersed granular features. This morphology suggests a layered growth pattern with some degree of nucleation and growth of smaller particles on the surface. Sample NCF in Fig. 8c shows agglomerated particles with some pore like craters, nickel doping generally results in moderate agglomeration (i.e. more agglomeration than other two

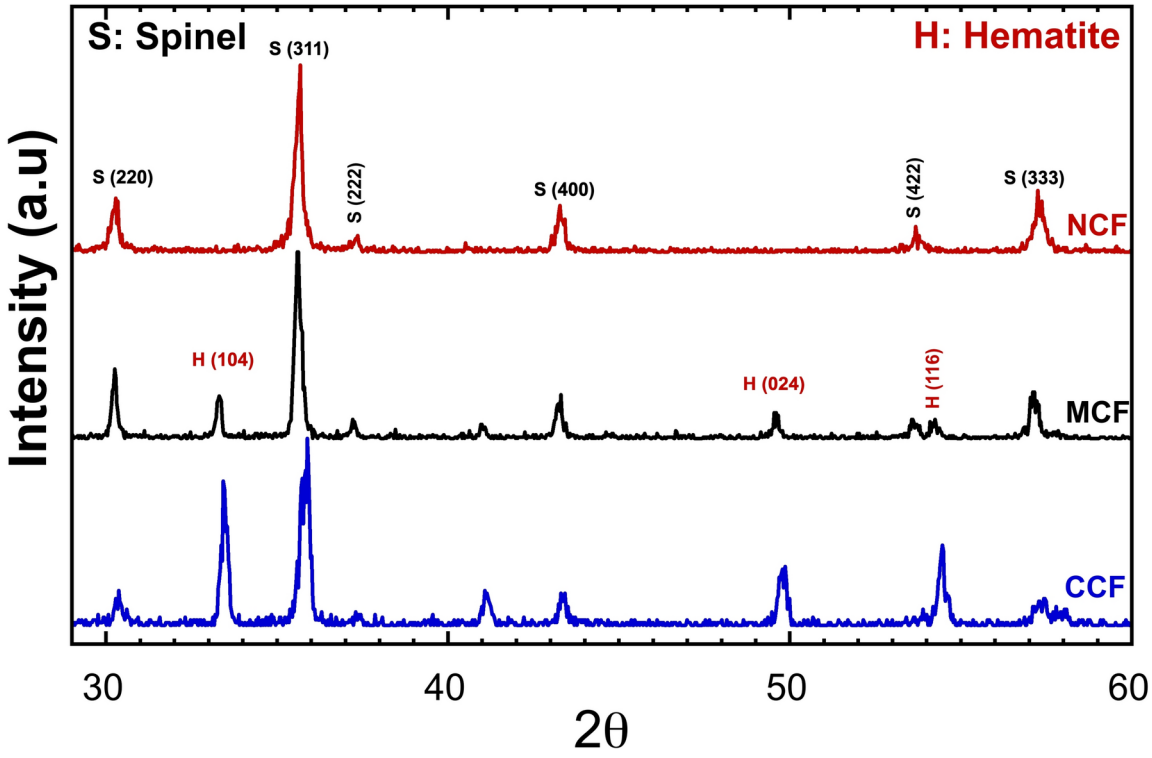

Fig. 7. XRD diffractograms of cobalt spinel ferrite samples substituted with Cr (CCF), Mn (MCF), and Ni (NCF).

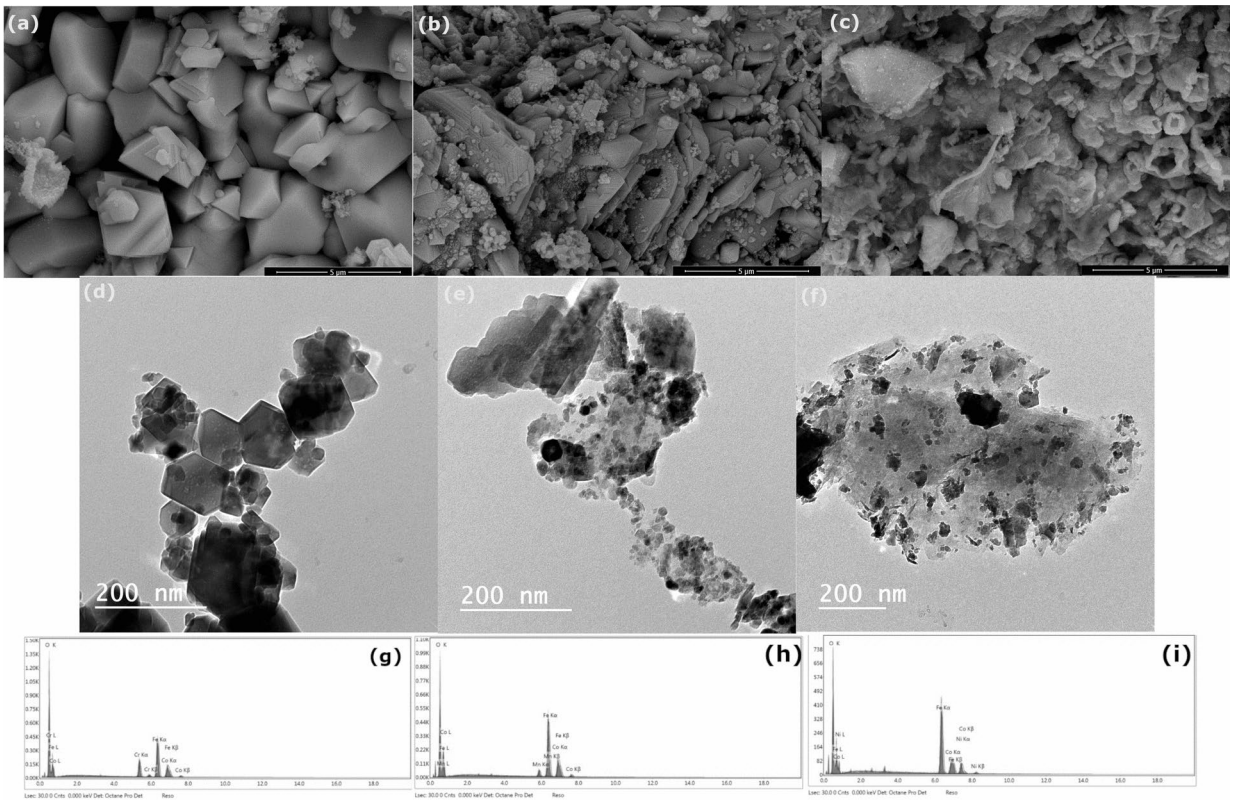

Fig. 8. SEM, TEM, and EDAX images of cobalt spinel ferrite samples substituted with Cr (CCF), Mn (MCF), and Ni (NCF).

samples). Figure 8d–f shows the TEM images of samples CCF, MCF, and NCF displaying a diverse range of shapes including polyhedral, elongated particles with sperical particles, and agglomerated particles. The EDAX images presented in Fig. 8g–i reveal the occurrence of oxygen, iron, and cobalt across all samples. Additionally, the CCF sample exhibits a distinct chromium peak, while the MCF sample shows a manganese peak, and the NCF sample displays a nickel peak. The particle shape and size of the powders were found to be influenced by the variations in their composition.

X-Ray photoelectron spectroscopy (XPS) analysis of samples prepared with different dopants.

XPS analysis was performed on the calcined CCF, MCF, and NCF samples to investigate the elemental composition and oxidation states of the constituents in substituted cobalt spinel ferrite. Figure 9a shows the XPS survey spectra, with peaks corresponding to Co2p, Fe2p, O1s and Cr2p, Mn2p, and Ni2p in samples CCF, MCF, and NCF; respectively. The high-resolution XPS spectra of Fe2p, shown in Fig. 9b, exhibits characteristic double peaks. These peaks are located at 710.3 eV, corresponding to $Fe2p_{3/2}$, and 723.9 eV, representing $Fe2p_{1/2}$. The observed spin–orbit splitting magnitude was approximately 13.6 eV, which is indicative of iron ions in the + 3 oxidation state[61]. Figure 9c displays the high-resolution XPS spectra for Co2p. Analysis of XPS data indicates the occurrence of $Co2p_{3/2}$ and $Co2p_{1/2}$ signals at 779.3 eV and 794.9 eV, respectively. Furthermore, two auxiliary peaks are detected at approximately 786.3 eV and 801.2 eV, which are typical of Co2p satellite peaks. The measured spin–orbit splitting value of about 15.6 eV indicated that the cobalt ions were in the + 2 oxidation state. The high-resolution XPS spectrum of O1s is shown in Fig. 9d. This spectrum reveals a dominant O1s peak near 529 eV, which is characteristic of lattice oxygen (O^{2-}) forming chemical bonds with metal ions in the crystal structure. Furthermore, a secondary peak was observed at about 532 eV, suggesting the existence of oxygen vacancies (Vo) in oxygen-deficient areas[31,40,41].

The high-resolution XPS spectra of Cr2p are depicted in Fig. 9e which reveals characteristic peaks in the Cr 2p region. The Cr $2p_{3/2}$ peak for Cr^{3+} is generally observed around 576 eV, while the Cr $2p_{1/2}$ peak appears at approximately 586 eV. The spin–orbit splitting between these two peaks is about 10 eV. The Cr $2p_{3/2}$ peak often exhibits an asymmetric shape due to multiplet splitting effects. The peak at 579 eV may be a satellite peak. In cobalt ferrite with chromium substitution, chromium is typically in the + 3 oxidation state, replacing some Fe^{3+} ions in the $CoFe_2O_4$ spinel lattice to maintain charge balance. The substituted cobalt ferrite's chemical composition can be represented as $CoCr_xFe_{2-x}O_4$, where x indicates the chromium substitution level[62].

The high-resolution XPS spectra of Mn2p are depicted in Fig. 9f. The spectra show peaks at 641.4 eV and at 652.9 eV which were assigned to $Mn2p_{3/2}$ and $Mn2p_{1/2}$, respectively. The approximate value of the spin–orbit splitting was 11.5 eV, which is indicative of the (+ 2) oxidation state of the Mn ions[61]. In manganese-substituted cobalt ferrite, manganese usually exhibits a + 2 or + 3 oxidation state. It substitutes either Co^{2+} or Fe^{3+} ions in the $CoFe_2O_4$ spinel structure, depending on synthesis conditions and desired properties. This substitution can be represented as $Co_{1-x}Mn_xFe_2O_4$ when Mn^{2+} replaces Co^{2+} or $CoMn_xFe_{2-x}O_4$ when Mn^{3+} replaces Fe^{3+}, with x indicating the substitution level. Manganese predominantly exists as Mn^{2+} in tetrahedral sites or Mn^{3+} in octahedral sites, although both states may coexist, influenced by synthesis method, temperature, and composition. Manganese incorporation significantly alters the ferrite's magnetic properties.

Figure 9g illustrates the high-resolution XPS spectra of Ni2p. The spectra reveal two distinct peaks: one at 854.7 eV and another at 871.9 eV. These peaks correspond to $Ni2p_{3/2}$ and Ni2p1/2, respectively[63].The approximate value of the spin–orbit splitting was 17.2 eV, which is indicative of the (+ 2) oxidation state of the Mn ions. Satellite peaks associated with each main peak, typically at 6–7 eV higher binding energy. In nickel-substituted cobalt ferrite, nickel typically maintains a + 2 oxidation state, replacing Co^{2+} ions in the $CoFe_2O_4$ spinel structure. The composition is represented by $Co_{1-x}Ni_xFe_2O_4$, where x indicates the nickel substitution level. Nickel, primarily existing as a divalent ion in tetrahedral positions, modifies the material's magnetic characteristics, electrical conductivity, and catalytic performance. These changes are influenced by synthesis methods, temperature conditions, and overall composition.

The XPS findings demonstrate the efficacy of the green microwave-assisted hydrothermal method in creating spinel ferrite with (+ 2) oxidation states of Co and Ni, and (+ 3) oxidation states of Fe and Cr ions and both oxidation states for Mn[61].

Magnetic properties of samples prepared with different dopants

A vibrating sample magnetometer (VSM) was employed to measure the magnetic properties at ambient temperature, with a magnetic field strength of 20 kG applied during the measurements. All samples showed ferromagnetic behavior as shown in Fig. 10. The Sample CCF exhibits a saturation magnetization (Ms) of approximately 23.53 emu/g, while its remnant magnetization (Mr) and coercivity (Hc) were measured at about 6.95 emu/g and 215 Oe, respectively. The Sample MCF exhibits a saturation magnetization (Ms) of approximately 55.15 emu/g, while its remnant magnetization (Mr) and coercivity (Hc) were measured at about 9.03 emu/g and 248 Oe, respectively. Sample NCF has a saturation magnetization (Ms) of ~ 45.85 emu/g and the remnant magnetization (Mr) and coercivity (Hc) were ~ 5.80 emu/g and 46 Oe, respectively. The literature suggests that incorporating both cobalt and other dopants modifies the magnetic characteristics in comparison with pure corresponding ferrite[13]. This effect is elaborated upon in the subsequent discussion. The Ms, Mr, and Hc values of $CoFe_2O_4$ are approximately 18 emu/g, 9.8 emu/g, and 1816 Oe, respectively[64]. In contrast, the Ms of $MnFe_2O_4$ is approximately 15 emu/g[5]. W. B. Mdlalose et al. compared $MnFe_2O_4$ and $Co_{0.5}Mn_{0.5}Fe_2O_4$ and the Ms were 49 emu/g and 63 emu/g and the Hc were 13 Oe and 53 Oe; respectively[65]. According to the findings of Duo et al., the obtained $CoFe_2O_4$ showed ferromagnetic behavior at room temperature, with M_s and M_r values of 47.1 emu/g and 27.5 emu/g, respectively. They observed a decrease in the Ms and Mr values of a $CoMn_{0.2}Fe_{1.8}O_4$ sample[66]. The introduction of chromium generally results in a reduction of the material's saturation magnetization. This

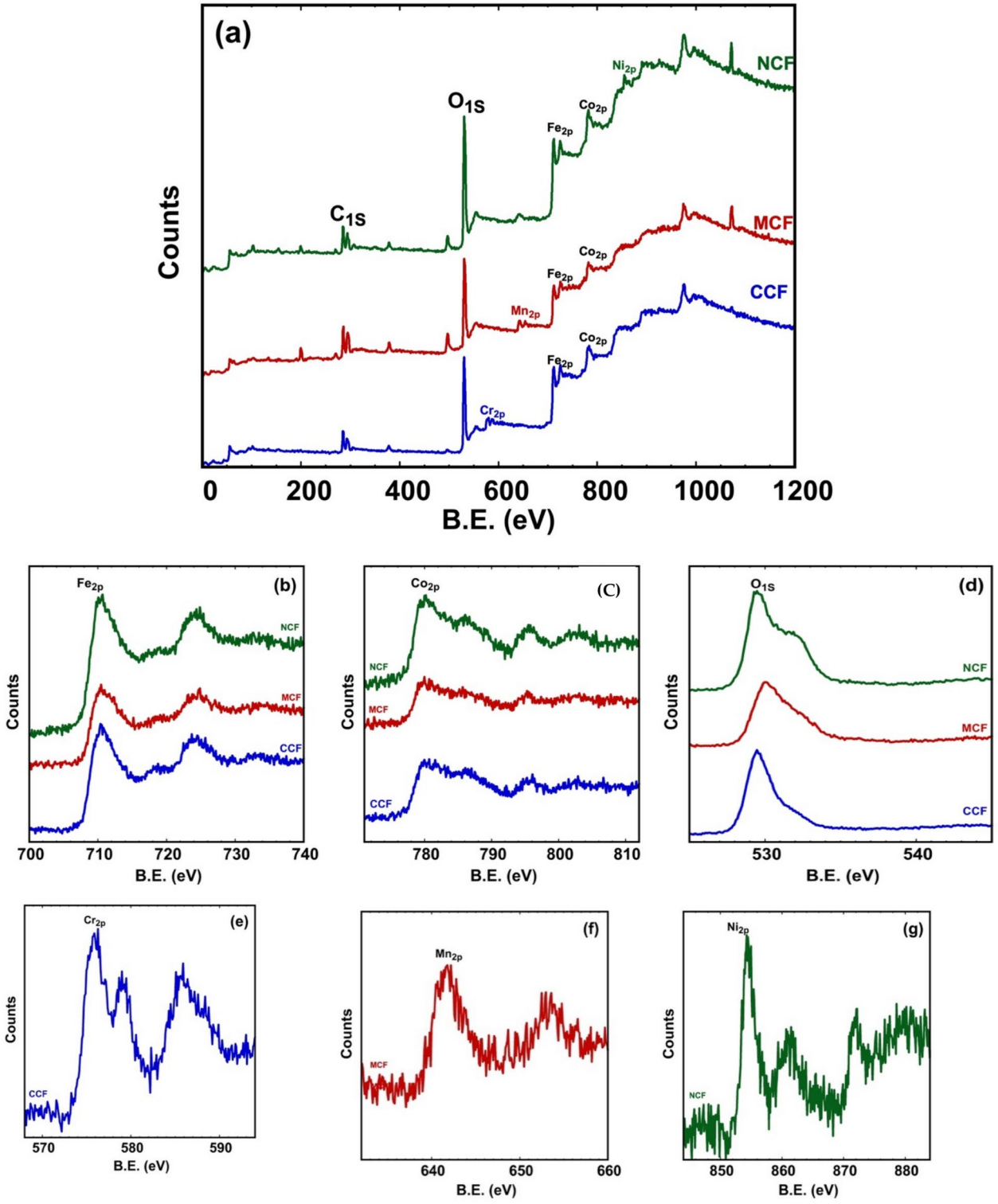

Fig. 9. XPS spectra (**a**) survey, high-resolution of (**b**) iron, (**c**) cobalt, (**d**) oxygen, (**e**) chromium, (**f**) manganese, and (**g**) nickel.

occurs because Cr^{3+} ions, which have 3 unpaired electrons, take the place of Fe^{3+} ions, which have 5 unpaired electrons, leading to a decrease in the number of unpaired electrons contributing to the net magnetic moment. Conversely, as the amount of manganese rises, the material's saturation magnetization increases. This effect is influenced by how Mn ions are distributed between octahedral and tetrahedral sites.

In this study, Cr, Mn, and Ni were chosen as replacements due to their significant influence on the structural and magnetic properties of cobalt spinel ferrite ($CoFe_2O_4$). These elements impact cation distribution,

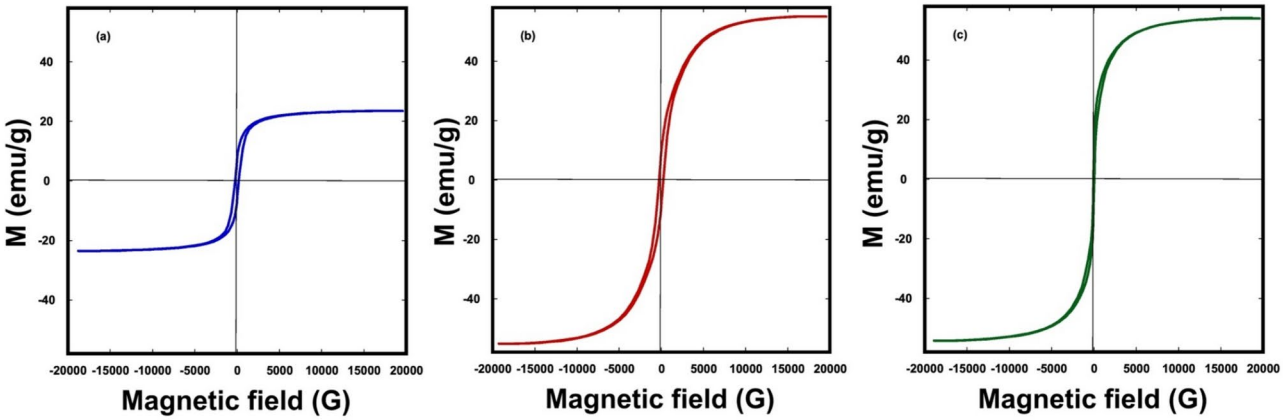

Fig. 10. M-H curves of of cobalt spinel ferrite samples substituted with Cr (CCF), Mn (MCF), and Ni (NCF).

oxidation states, and magnetic interactions, leading to specific effects on the material's stability and magnetic characteristics. Nickel (Ni^{2+}) was selected because its ionic radius (0.69 Å) closely matches that of Co^{2+} (0.74 Å) and it prefers octahedral sites, allowing for a smooth substitution that strengthens the pure cubic spinel phase without forming hematite (Fe_2O_3). This enhances the material's thermal stability while slightly reducing the saturation magnetization (Ms) (46 emu/g in the NCF sample compared to 55 emu/g in the MCF sample) due to changes in superexchange interactions. On the other hand, manganese (Mn) exhibits multiple oxidation states (+2, +3, +4), increasing the likelihood of secondary phase formation such as hematite. Mn^{2+} tends to occupy tetrahedral sites, while Mn^{3+} is found in octahedral positions, creating complex magnetic interactions that can alter the coercivity (Hc). Chromium (Cr^{3+}) was chosen because it mainly replaces Fe^{3+} in octahedral sites, but its smaller ionic radius (0.62 Å) causes lattice distortion, affecting exchange interactions and decreasing Ms (23 emu/g). Additionally, Cr^{3+} has a lower magnetic moment than Fe^{3+}, weakening the overall superexchange interactions within the spinel structure. The selection of these elements aimed to explore their role in stabilizing the spinel structure, modifying magnetic properties, and understanding phase formation mechanisms, which are crucial for improving ferrites for various technological applications[18,67,68].

Antimicrobial

Cobalt ferrite ($CoFe_2O_4$) is a well-known spinel ferrite material with potential antimicrobial applications. Substituting a portion of the cobalt ions with other transition metals can modify its properties, potentially enhancing its antimicrobial activity. CFU (Colony-Forming Units) is a measure of the number of viable bacteria or other microorganisms in a sample. A reduction in CFU typically indicates a decrease in the number of viable organisms. Figure 11 represents CFU reduction of bacterial strains after incubation applying the tested samples (CCF, MCF, and NCF) using shake flask method by turbidimetric analysis. Mn substituted Cobalt ferrite shows moderate CFU reduction against *Escherichia coli*, *Staphylococcus aureus*, and *Candida albicansa*. Sample NCF, nickel substituted Cobalt ferrite shows lower CFU reduction against *Escherichia coli* and *Candida albicansa* than sample MCF sample while it shows higher CFU reduction against *Staphylococcus aureus*. Finally, sample CCF shows best results of CFU reduction against *Escherichia coli*, *Staphylococcus aureus*, and *Candida albicansa*. Sample CFF was used in CFU reduction of pathogenic strains after incubation applying the best tested samples using shake flask method standard by viable plate count analysis as shown in Fig. 12.

Figure 12 shows the comparison between images of blank meduim, in presence of control, and in presence of sample CCF against *Escherichia coli*, *Staphylococcus aureus*, and *Candida albicansa*. The images show a decrease of pathogenic growth in presence of sample CCF. The sample shows high CFU reduction % against *Escherichia coli*, *Staphylococcus aureus*, and *Candida albicansa* (i.e. 87, 83, and 86%). Substituted cobalt ferrites can demonstrate antimicrobial properties through several pathways, such as: producing reactive oxygen species (ROS), compromising cell membrane integrity, or disrupting cellular metabolic functions. This capability enables potential uses in various fields such as eliminating harmful microorganisms from water sources, applying protective layers on implants or surgical tools to prevent bacterial growth, and integrating into textiles for creating antimicrobial garments or protective wear.

The Cr-substituted spinel (CCF) exhibited exceptional antibacterial performance, primarily due to its increased generation of reactive oxygen species (ROS). These ROS create oxidative stress, damaging bacterial cell membranes, proteins, and DNA. Cr^{3+} ions have a higher charge density than Mn^{2+} and Ni^{2+}, allowing for stronger electrostatic interactions with the negatively charged bacterial cell walls. This interaction leads to membrane disruption and higher bacterial cell death rates. Additionally, the smaller ionic radius of Cr^{3+} (0.62 Å) compared to Mn^{2+} (0.83 Å) and Ni^{2+} (0.69 Å) results in greater lattice structure distortion, which enhances surface reactivity and antibacterial properties. In contrast, the Mn-substituted spinel (MCF) showed moderate antibacterial activity, likely because manganese's multiple oxidation states (+2, +3, +4) are less effective at producing ROS. The Ni-substituted spinel (NCF) demonstrated selective antibacterial effects, especially against Staphylococcus aureus, possibly due to its preference for octahedral sites, affecting its surface interactions and

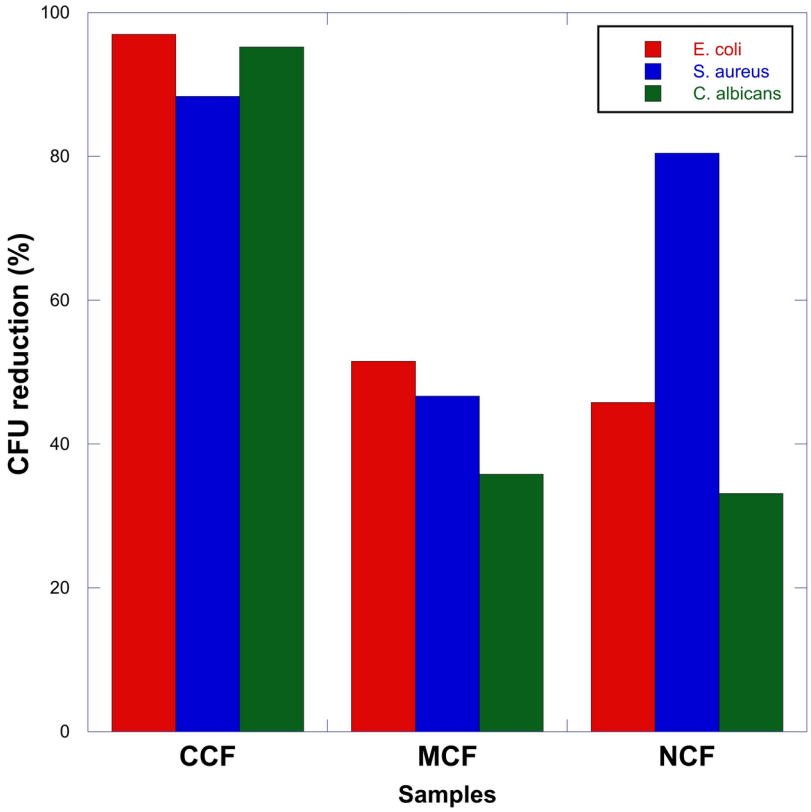

Fig. 11. (%) CFU reduction of bacterial strains after incubation applying the tested samples using shake flask method Turbidimetric analysis.

ROS production. These factors account for the superior effectiveness of CCF, while MCF and NCF show varying levels of antibacterial activity against different bacterial strains[69,70].

Conclusions

The synthesis of spinel ferrite through a henna-green/microwave-assisted hydrothermal technique offers several advantages, including the ability to heat the material using microwave radiation rapidly and efficiently and a controlled environment for the formation of spinel ferrite, leading to a well-defined and highly uniform structure. Furthermore, this method employs green synthesis principles that minimize the use of toxic chemicals and hazardous solvents, making it a more sustainable and environmentally friendly approach for nanocomposite synthesis. Spinel ferrite nanocomposites have a cubic-face crystal structure of spinel ferrite and hematite. The morphological diversity of the cobalt-manganese spinel ferrite nanocomposites was remarkable, exhibiting rod-like, flower-like, and polygonal shapes. Analysis of the samples using XPS revealed that cobalt, nickel, and manganese were present in the + 2-oxidation state, whereas iron and chromium exhibited the + 3-oxidation state. Analysis of magnetic properties revealed that the produced nanocomposites displayed ferromagnetic characteristics, with saturation magnetization (Ms) ranging from 23.53 to 55.15 emu/g. The incorporation of chromium demonstrated superior antimicrobial efficacy against *Escherichia coli*, *Staphylococcus aureus*, and *Candida albicans*. Future investigations will examine the synthesis methodology with diverse compositions and various dopants.

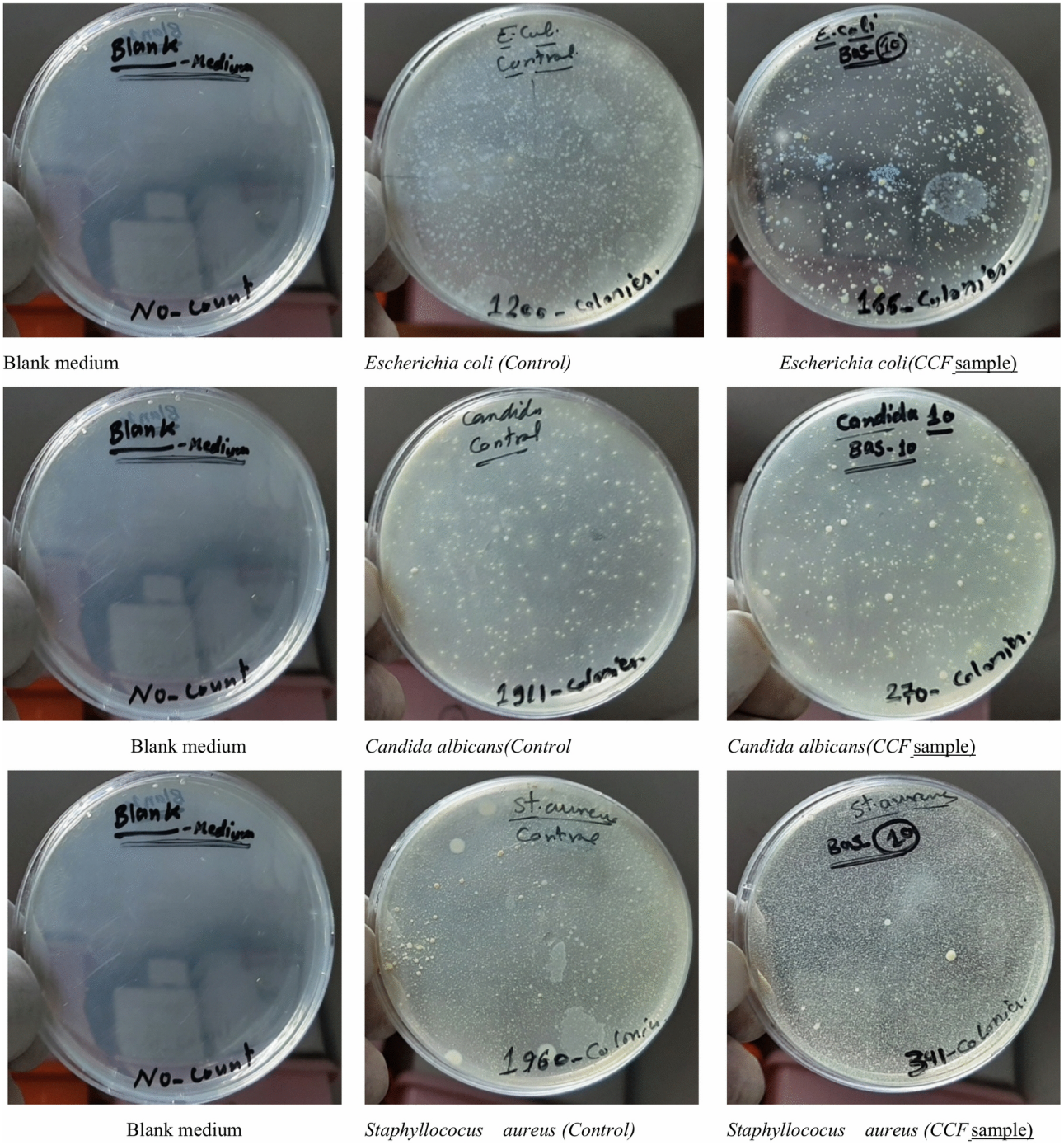

Blank medium | *Escherichia coli (Control)* | *Escherichia coli(CCF sample)*

Blank medium | *Candida albicans(Control* | *Candida albicans(CCF sample)*

Blank medium | *Staphyllococus aureus (Control)* | *Staphyllococus aureus (CCF sample)*

Fig. 12. Effect of CCF sample on (%) CFU reduction of pathogenic strains applying plate count analysis.

Data availability

All data generated or analyzed during this study are included in this published article.

Received: 5 February 2025; Accepted: 30 April 2025
Published online: 13 May 2025

References

1. Kombaiah, K. et al. A Green approach: synthesis, characterization and opto-magnetic properties of MgxMn1−xFe2O4 spinel nanoparticles. *J. Mater. Sci. Mater. Electron.* **28**, 10321–10329. https://doi.org/10.1007/s10854-017-6800-2 (2017).
2. Davydov, A. S. et al. Promising magnetic nanoradiosensitizers for combination of tumor hyperthermia and X-ray therapy: Theoretical calculation. *J. Appl. Phys.* **2021**, 129. https://doi.org/10.1063/5.0032843 (2021).

3. Lee, S. W. et al. Self-heating characteristics of cobalt ferrite nanoparticles for hyperthermia application. *J. Magn. Magn. Mater.* **310**, 2868–2870. https://doi.org/10.1016/j.jmmm.2006.11.080 (2007).
4. Manohar, A., Chintagumpala, K. & Kim, K. H. Mixed Zn–Ni spinel ferrites: Structure, magnetic hyperthermia and photocatalytic properties. *Ceram. Int.* **47**, 7052–7061. https://doi.org/10.1016/j.ceramint.2020.11.056 (2021).
5. Alhalili, Z. & Abdelrahman, E. A. Facile synthesis and characterization of manganese ferrite nanoparticles for the successful removal of safranine T dye from aqueous solutions. *Inorganics* **2024**, 12. https://doi.org/10.3390/inorganics12010030 (2024).
6. Tamboli, Q. Y. et al. Green synthesis of cobalt ferrite nanoparticles: an emerging material for environmental and biomedical applications. *J. Nanomater.* **2023**, 1–15. https://doi.org/10.1155/2023/9770212 (2023).
7. Chaudhari, A. et al. Dye degradation and antimicrobial applications of manganese ferrite nanoparticles synthesized by plant extracts. *Chem. Phys. Impact* **2022**, 5. https://doi.org/10.1016/j.chphi.2022.100098 (2022).
8. Al-Zahrani, S. A. et al. Influence of Ce3+ on the structural, morphological, magnetic, photocatalytic and antibacterial properties of spinel MnFe2O4 nanocrystallites prepared by the combustion route. *Crystals* **2022**, 12. https://doi.org/10.3390/cryst12020268 (2022).
9. Pietrzyk, P. et al. Green composites based on volcanic red algae Cyanidiales, cellulose, and coffee waste biomass modified with magnetic nanoparticles for the removal of methylene blue. *Environ. Sci. Pollut. Res. Int.* **30**, 62689–62703. https://doi.org/10.1007/s11356-023-26425-3 (2023).
10. Bharathi, S. D. & Babu, D. R. Synthesis, characterization and antimicrobial activity of Manganese ferrite nanoparticles. *Mater. Sci. Eng. B* **2024**, 300. https://doi.org/10.1016/j.mseb.2023.117051 (2024).
11. Ehi-Eromosele, O. Synthesis and evaluation of the antimicrobial potentials of cobalt doped- and magnesium ferrite spinel nanoparticles. *Bull. Chem. Soc. Ethiopia* **2018**, 32 (2018).
12. Venkatasubramanian, R. & Misra, R. D. K. Comparative study of antimicrobial and photocatalytic activity in titania encapsulated composite nanoparticles with different dopants. *Mater. Sci. Technol.* **24**, 7 (2008).
13. Salih, S. J. & Mahmood, W. M. Review on magnetic spinel ferrite (MFe(2)O(4)) nanoparticles: From synthesis to application. *Heliyon* **9**, e16601. https://doi.org/10.1016/j.heliyon.2023.e16601 (2023).
14. Dippong, T., Levei, E. A. & Cadar, O. Recent advances in synthesis and applications of MFe(2)O(4) (M = Co, Cu, Mn, Ni, Zn) nanoparticles. *Nanomaterials (Basel)* **2021**, 11. https://doi.org/10.3390/nano11061560 (2021).
15. Liu, Y., Chen, Y., Zhu, X., Zhao, P. & Ren, W. Determination of quinolone antibiotics in surface water by MnFe2O4@TiO2 magnetic solid phase extraction-high performance liquid chromatography. *Microchem. J.* **2024**, 204. https://doi.org/10.1016/j.microc.2024.111090 (2024).
16. Yan, Z., FitzGerald, S., Crawford, T. M. & Mefford, O. T. Manganese and cobalt substituted ferrite nanoparticles synthesized via a seed-mediated drip method. *J. Phys. Mater.* **2021**, 4. https://doi.org/10.1088/2515-7639/abfcd5 (2021).
17. Keswani, B. C., Patil, S. I., Kolekar, Y. D. & Ramana, C. V. Improved magnetostrictive properties of cobalt ferrite (CoFe2O4) by Mn and Dy co-substitution for magneto-mechanical sensors. *J. Appl. Phys.* **2019**, 126. https://doi.org/10.1063/1.5114815 (2019).
18. Monisha, P., Priyadharshini, P., Gomathi, S. S. & Pushpanathan, K. Influence of Mn dopant on the crystallite size, optical and magnetic behaviour of CoFe2O4 magnetic nanoparticles. *J. Phys. Chem. Solids* **2021**, 148. https://doi.org/10.1016/j.jpcs.2020.109654 (2021).
19. Datt, G., Kotabage, C. & Abhyankar, A. C. Ferromagnetic resonance of NiCoFe(2)O(4) nanoparticles and microwave absorption properties of flexible NiCoFe(2)O(4)-carbon black/poly(vinyl alcohol) composites. *Phys. Chem. Chem. Phys.* **19**, 20699–20712. https://doi.org/10.1039/c7cp03953k (2017).
20. Vadivel, M., Ramesh Babu, R., Sethuraman, K., Ramamurthi, K. & Arivanandhan, M. Synthesis, structural, dielectric, magnetic and optical properties of Cr substituted CoFe2O4 nanoparticles by co-precipitation method. *J. Magn. Magn. Mater.* **362**, 122–129. https://doi.org/10.1016/j.jmmm.2014.03.016 (2014).
21. Singh, R., Singh, N., Singh, J., Balaji, G. & Gajbhiye, N. Effect of partial substitution of Cr on electrocatalytic properties of CoFe2O4CoFe2O4 towards O2O2-evolution in alkaline medium☆. *Int. J. Hydrogen Energy* **31**, 701–707. https://doi.org/10.1016/j.ijhydene.2005.07.003 (2006).
22. Shinde, V. S. et al. Structure, morphology, cation distribution and magnetic properties of Cr3+-substituted CoFe2O4 nanoparticles. *J. Supercond. Novel Magn.* **32**, 945–955. https://doi.org/10.1007/s10948-018-4778-5 (2018).
23. Verma, K. C., Goyal, N., Singh, M., Singh, M. & Kotnala, R. K. Hematite α-Fe2O3 induced magnetic and electrical behavior of NiFe2O4 and CoFe2O4 ferrite nanoparticles. *Results Phys.* **2019**, 13. https://doi.org/10.1016/j.rinp.2019.102212 (2019).
24. Masahiko Naoe, N. M. Deposition of single-layer CoFe204and multilayer CoFe204/Fe203with large Ms and high Hc using vacuum arc evaporation. *J. Magn. Magn. Mater.* **155**, 3 (1996).
25. Lv, H. et al. Coin-like alpha-Fe2O3@CoFe2O4 core-shell composites with excellent electromagnetic absorption performance. *ACS Appl. Mater. Interfaces* **7**, 4744–4750. https://doi.org/10.1021/am508438s (2015).
26. Huang, G. et al. Hierarchical NiFe2O4/Fe2O3 nanotubes derived from metal organic frameworks for superior lithium ion battery anodes. *J. Mater. Chem. A* **2**, 8048–8053. https://doi.org/10.1039/c4ta00200h (2014).
27. Vinosha, P. A. et al. Exploring the influence of varying pH on structural, electro-optical, magnetic and photo-Fenton properties of mesoporous ZnFe2O4 nanocrystals. *Environ. Pollut.* **272**, 115983. https://doi.org/10.1016/j.envpol.2020.115983 (2021).
28. Manohar, A. et al. Comprehensive study of CeO2/CuFe2O4 nanocomposites: Structural, EPR, magnetic, electrochemical, and cytotoxicity properties. *Mater. Charact.* https://doi.org/10.1016/j.matchar.2024.114471 (2024).
29. López Medina, J. A. et al. Magnetic, structural, and morphological properties behavior of Ni1−xCoxFe2O4 magnetic nanoparticles: Theoretical and experimental study. *Mater. Charact.* https://doi.org/10.1016/j.matchar.2024.114296 (2024).
30. Al Sdran, N., Chandekar, K. V., Ansari, S. A. & Shkir, M. Novel Mo: CoFe2O4 nanoparticles combustion synthesis for opto-magneto-electrochemical applications: A systematic analysis. *Mater. Charact.* https://doi.org/10.1016/j.matchar.2024.114514 (2024).
31. Liu, P., Yao, Z., Zhou, J., Yang, Z. & Kong, L. B. Small magnetic Co-doped NiZn ferrite/graphene nanocomposites and their dual-region microwave absorption performance. *J. Mater. Chem. C* **4**, 9738–9749. https://doi.org/10.1039/c6tc03518c (2016).
32. Al-Yunus, A. et al. Effect of synthesis conditions on CuO–NiO nanocomposites synthesized via saponin-green/microwave assisted-hydrothermal method. *Nanomaterials (Basel)* https://doi.org/10.3390/nano14030308 (2024).
33. Hassanpour, M., Safardoust, H., Ghanbari, D. & Salavati-Niasari, M. Microwave synthesis of CuO/NiO magnetic nanocomposites and its application in photo-degradation of methyl orange. *J. Mater. Sci. Mater. Electron.* **27**, 2718–2727. https://doi.org/10.1007/s10854-015-4082-0 (2015).
34. Wang, W.-W., Zhu, Y.-J., Cheng, G.-F. & Huang, Y.-H. Microwave-assisted synthesis of cupric oxide nanosheets and nanowhiskers. *Mater. Lett.* **60**, 609–612. https://doi.org/10.1016/j.matlet.2005.09.056 (2006).
35. Safi, R., Ghasemi, A., Shoja-Razavi, R. & Tavousi, M. The role of pH on the particle size and magnetic consequence of cobalt ferrite. *J. Magn. Magn. Mater.* **396**, 288–294. https://doi.org/10.1016/j.jmmm.2015.08.022 (2015).
36. Li, R., Liu, J., Xu, L. & Zhou, J. Microwave idrothermal synthesis of magnesium-aluminium spinel. *Ceram. Int.* **46**, 29207–29211. https://doi.org/10.1016/j.ceramint.2020.08.094 (2020).
37. Yew, Y. P. et al. Green biosynthesis of superparamagnetic magnetite Fe3O4 nanoparticles and biomedical applications in targeted anticancer drug delivery system: A review. *Arab. J. Chem.* **13**, 2287–2308. https://doi.org/10.1016/j.arabjc.2018.04.013 (2020).
38. Wani, T. A. & Suresh, G. Plant-mediated green synthesis of magnetic spinel ferrite nanoparticles: a sustainable trend in nanotechnology. *Adv. Sustain. Syst.* https://doi.org/10.1002/adsu.202200035 (2022).

39. Divakara, S. G. & Mahesh, B. A comprehensive review on current trends in greener and sustainable synthesis of ferrite nanoparticles and their promising applications. *Results Eng.* https://doi.org/10.1016/j.rineng.2023.101702 (2024).
40. Jasim, S. A. et al. Green synthesis of spinel copper ferrite (CuFe2O4) nanoparticles and their toxicity. *Nanotechnol. Rev.* **11**, 2483–2492. https://doi.org/10.1515/ntrev-2022-0143 (2022).
41. Ameen, F. Green synthesis spinel ferrite nanosheets and their cytotoxicity and antibacterial activity. *Biomass Convers. Bioref.* https://doi.org/10.1007/s13399-022-03638-z (2022).
42. Khantamat, O. et al. Safety and bioactivity assessment of aqueous extract of Thai Henna (*Lawsonia inermis* Linn) Leaf. *J. Toxicol. Environ. Health A* **84**, 298–312. https://doi.org/10.1080/15287394.2020.1866129 (2021).
43. Taghavi Fardood, S., Ramazani, A., Asiabi, P. A. & Joo, S. W. A. Novel green synthesis of copper oxide nanoparticles using a henna extract powder. *J. Struct. Chem.* **59**, 1737–1743. https://doi.org/10.1134/s0022476618070302 (2018).
44. Brixi, N. K., Cherif, R., Bezzar, A., Sail, L. & Aït-Mokhtar, A. Effectiveness of henna leaves extract and its derivatives as green corrosion inhibitors of reinforcement steel exposed to chlorides. *Eur. J. Environ. Civ. Eng.* https://doi.org/10.1080/19648189.2021.1925159 (2021).
45. Musa, M. S. M. et al. Application of henna extract in minimizing surfactant adsorption on quartz sand in saline condition: A sacrificial agent approach. *SN Appl. Sci.* https://doi.org/10.1007/s42452-019-0870-0 (2019).
46. Imanipour, P., Hasani, S., Seifoddini, A. & Nabialek, M. Synthesis and characterization of zinc and vanadium co-substituted CoFe2O4 nanoparticles synthesized by using the sol-gel auto-combustion method. *Nanomaterials (Basel)* https://doi.org/10.3390/nano12050752 (2022).
47. Šuljagić, M. et al. The influence of the starch coating on the magnetic properties of nanosized cobalt ferrites obtained by different synthetic methods. *Mater. Res. Bull.* https://doi.org/10.1016/j.materresbull.2020.111117 (2021).
48. Sarala, E., Madhukara Naik, M., Vinuth, M., Rami Reddy, Y. V. & Sujatha, H. R. Green synthesis of Lawsonia inermis-mediated zinc ferrite nanoparticles for magnetic studies and anticancer activity against breast cancer (MCF-7) cell lines. *J. Mater. Sci. Mater. Electron.* **31**, 8589–8596. https://doi.org/10.1007/s10854-020-03394-8 (2020).
49. Kurmude, D. V., Barkule, R. S., Raut, A. V., Shengule, D. R. & Jadhav, K. M. X-ray diffraction and cation distribution studies in zinc-substituted nickel ferrite nanoparticles. *J. Supercond. Novel Magn.* **27**, 547–553. https://doi.org/10.1007/s10948-013-2305-2 (2013).
50. Pandit, A. A., Shengule, D. R. & Jadhav, K. M. Magnetic and dielectric properties of Mg1+x Mnx Fe2−2x O4 ferrite system. *J. Mater. Sci.* **40**, 6 (2005).
51. Mallesh, S. & Srinivas, V. Evolution of structure and magnetic properties in MnZn ferrite-silica nanocomposites fabricated by sol–gel method. *J. Mater. Sci. Mater. Electron.* **32**, 4862–4871. https://doi.org/10.1007/s10854-020-05225-2 (2021).
52. Zainuri, M. Hematite from natural iron stones as microwave absorbing material on X-band frequency ranges. In *Proceedings of the 3rd International Conference on Functional Materials Science*, 5 (2016).
53. Ramay, S. M., Atiq, S., Siddiqi, S. A. & Naseem, S. Influence of temperature on structural and magnetic properties of Co0·5Mn0·5Fe2O4 ferrites. *Bull. Mater. Sci.* **34**, 5 (2011).
54. Fernandes de Medeiros, I. A., Lopes-Moriyama, A. L. & de Souza, C. P. Effect of synthesis parameters on the size of cobalt ferrite crystallite. *Ceram. Int.* **43**, 3962–3969. https://doi.org/10.1016/j.ceramint.2016.10.105 (2017).
55. Cote, L. J., Wilkinson, A. P. & Zhang, Z. J. Continuous hydrothermal synthesis and crystallization of magnetic oxide nanoparticles. *J. Mater. Res.* **17**, 7 (2002).
56. Pasandi Pour, A. & Farahbakhsh, H. *Lawsonia inermis* L. leaves aqueous extract as a natural antioxidant and antibacterial product. *Nat. Prod. Res.* **34**, 3399–3403. https://doi.org/10.1080/14786419.2019.1569006 (2020).
57. Abid, M. A. & Kadhim, D. A. Novel comparison of iron oxide nanoparticle preparation by mixing iron chloride with henna leaf extract with and without applied pulsed laser ablation for methylene blue degradation. *J. Environ. Chem. Eng.* https://doi.org/10.1016/j.jece.2020.104138 (2020).
58. Kershi, R. M. & Aldirham, S. H. Transport and dielectric properties of nanocrystallite cobalt ferrites: Correlation with cations distribution and crystallite size. *Mater. Chem. Phys.* https://doi.org/10.1016/j.matchemphys.2019.121902 (2019).
59. Galindo, R. et al. Comparison of different methodologies for obtaining nickel nanoferrites. *J. Magn. Magn. Mater.* **361**, 118–125. https://doi.org/10.1016/j.jmmm.2014.02.091 (2014).
60. Zhang, Q. et al. CuO nanostructures: Synthesis, characterization, growth mechanisms, fundamental properties, and applications. *Prog. Mater Sci.* **60**, 208–337. https://doi.org/10.1016/j.pmatsci.2013.09.003 (2014).
61. Moulder, J. F., Stickle, W. F., E.'Sobol, P., Bomben, K.D. *Handbook of X-ray Photoelectron Spectroscopy* (1993).
62. Xu, Y. et al. Enhancing bifunctional catalytic activity of cobalt-nickel sulfide spinel nanocatalysts through transition metal doping and its application in secondary zinc-air batteries. *RSC Adv.* **10**, 41871–41882. https://doi.org/10.1039/d0ra08363a (2020).
63. Shao, L. et al. Microstructure, XPS and magnetic analysis of Al-doped nickel–manganese–cobalt ferrite. *J. Mater. Sci. Mater. Electron.* **32**, 20474–20488. https://doi.org/10.1007/s10854-021-06557-3 (2021).
64. Mahdy, M. A., Azab, A. A., El Zawawi, I. K. & Turky, G. Tailoring ZnO/CoFe2O4 nanocomposites: structure, optical, dielectric and magnetic study. *Phys. Scripta* https://doi.org/10.1088/1402-4896/aca5bc (2022).
65. Mdlalose, W. B., Mokhosi, S. R., Dlamini, S., Moyo, T. & Singh, M. Effect of chitosan coating on the structural and magnetic properties of MnFe2O4 and Mn0.5Co0.5Fe2O4 nanoparticles. *AIP Adv.* https://doi.org/10.1063/1.5007760 (2018).
66. Dou, R., Cheng, H., Ma, J. & Komarneni, S. Manganese doped magnetic cobalt ferrite nanoparticles for dye degradation via a novel heterogeneous chemical catalysis. *Mater. Chem. Phys.* https://doi.org/10.1016/j.matchemphys.2019.122181 (2020).
67. Safi, R., Ghasemi, A., Shoja-Razavi, R. & Tavousi, M. The role of pH on the particle size and magnetic consequence of cobalt ferrite. *J. Magn. Magn. Mater.* **396**, 7 (2015).
68. Deshmukh, S. P., Sanadi, K. R., Diggikar, R. S., Koli, V. B. & Mali, A. V. Structural, magnetic, and electrical properties of manganese-substituted magnesium chromate spinel structure. *J. Mater. Sci. Mater. Electron.* **32**, 6810–6819. https://doi.org/10.1007/s10854-021-05386-8 (2021).
69. Velho-Pereira, S., Noronha, A., Mathias, A., Zakane, R., Naik, V., Naik, P., Salker, A. V., & Naik, S. R. (2015) Antibacterial action of doped CoFe2O4 nanocrystals on multidrug resistant bacterial strains. *Mater. Sci. Eng. C Mater. Biol. Appl.* **52**, 6. https://doi.org/10.1016/j.msec.2015.03.046.
70. Kaur, S. et al. Spinel nanoferrite (CoFe2O4): The impact of Cr doping on its structural, surface morphology, magnetic, and antibacterial activity traits. *Opt. Mater.* https://doi.org/10.1016/j.optmat.2022.113026 (2022).

Acknowledgements

The authors extend their appreciation to the Deanship of Scientific Research, Vice Presidency for Graduate Studies and Scientific Research, King Faisal University, Saudi Arabia [Grant No. KFU250203

Author contributions

Conceptualization, M.H.; methodology, B.G. and M.H.; data curation, B.G. and M.H.; writing—original draft preparation, M.H.; editing, M.H.; visualization, M.H.; supervision, M.H. Project administration, M.H. Funding acquisition: M.H. All the authors have read and agreed to the published version of the manuscript.

Funding
This work was supported by the Deanship of Scientific Research, Vice Presidency for Graduate Studies and Scientific Research, King Faisal University, Saudi Arabia [Grant No. KFU250203.

Declarations

Competing interests
The authors declare no competing interests.

Additional information
Correspondence and requests for materials should be addressed to M.H.

Reprints and permissions information is available at www.nature.com/reprints.

Publisher's note Springer Nature remains neutral with regard to jurisdictional claims in published maps and institutional affiliations.